

Observation of moiré trapped biexciton through sub-diffraction-limit probing using hetero-bilayer on nanopillar

Mayank Chhaperwal^{1,||}, Suman Chatterjee^{1,2,||}, Suchithra Puliassery¹,
Jyothsna Konkada Manattayil¹, Rabindra Biswas^{1,3}, Patrick Hays⁴, Seth Ariel Tongay⁴,
Varun Raghunathan¹, and Kausik Majumdar^{1*}

¹Department of Electrical Communication Engineering,
Indian Institute of Science, Bangalore 560012, India

²Currently at Quantum Matter Institute, University of British Columbia,
Vancouver, British Columbia V6T 1Z4, Canada

³Currently at Department of Physics, Emory University, Atlanta, USA

⁴Materials Science and Engineering, School for Engineering of Matter,
Transport and Energy, Arizona State University, Tempe, Arizona 85287, United States

^{||}These authors contributed equally

*Corresponding author, email: kausikm@iisc.ac.in

Abstract

The ability to tune the degree of interaction among particles at the nanoscale is highly intriguing. The spectroscopic signature of such interaction is often subtle and requires special probes to observe. To this end, inter-layer excitons trapped in the periodic potential wells of a moiré superlattice offer rich interaction physics, specifically due to the presence of both attractive and repulsive components in the interaction. Here we show that the Coulomb force between two inter-layer excitons switches from repulsive to attractive when the length scale reduces from inter-moiré-pocket to intra-moiré-pocket in a WS_2/WSe_2 hetero-bilayer - thanks to the complex competition between direct and exchange interaction. The finding is a departure from the usual notion of repelling inter-layer excitons due to layer polarization. This manifests as the simultaneous observation of an anomalous superlinear power-law of moiré exciton and a stabilization of moiré trapped biexciton. The experimental observation

is facilitated by placing the hetero-bilayer on a polymer-nanopillar/gold-film stack which significantly reduces the inhomogeneous spectral broadening by selectively probing a smaller ensemble of moiré pockets compared with a flat sample. This creates an interesting platform to explore interaction among moiré trapped excitons and higher order quasiparticles.

2D Exciton, while being overall charge neutral, is a field-polarizable quasiparticle composed of a negatively charged electron and a positively charged hole that are strongly bound to each other [1, 2]. The presence of oppositely charged particles in an exciton makes the inter-exciton interaction highly intriguing due to the complex interplay between attractive and repulsive forces through direct and exchange Coulomb interactions. In a monolayer, two excitons in proximity minimize the total energy by reconstruction (see left part of Figure 1a), forming a biexciton that has a negative binding energy [3, 4]. In contrast, in the case of inter-layer exciton (ILE) of hetero-bilayer, such a reconstruction is restricted by the strong layer polarization (electron and hole residing in opposite layers, see right part of Figure 1a). As a result, inter-exciton interaction often turns out to be repulsive in nature [5–7], making the stabilization of inter-layer biexciton difficult. Such a repulsive interaction has been widely reported through the observation of a blue shift of the ILE emission energy with an increase in the incident optical power [5, 7].

In a moiré superlattice, the potential landscape can force two excitons to be trapped inside a single potential well having a diameter on the order of a few nanometers (see Figure 1b,c). The dipolar repulsion between the two ILE inside a moiré well has been recently shown to create ladder-like higher energy excitonic states [8, 9]. This exciton-exciton proximity, coupled with the innate out-of-plane confinement in the ultra-thin layers, results in a competition between the direct and exchange Coulomb interaction. An interesting question to pose here is whether the exchange interaction can overcome the direct repulsive interaction and stabilize the biexciton in a moiré well.

To this end, our variational calculations (discussed later and also in **Methods**) suggest that such stabilization is indeed possible for the spatially antisymmetric (triplet) biexciton configuration (see Figure 1d-f). Figure 1d shows the calculated binding energy (E_b) of the biexciton as a function of the separation (ρ) between the centers of mass (COM) of the two constituent excitons and the width (ζ) of the exciton wave packets (ρ and ζ are defined in Figure 1b). E_b becomes negative and exhibits a minimum for small ρ and ζ at a length scale similar to the size of the moiré well, suggesting the possibility of experimental observation of moiré trapped biex-

citon. On the other hand, the potential barrier between two neighboring moiré wells suppresses the wave function overlap (bottom panel of Figure 1b), and thus, inter-moiré well excitonic interaction remains repulsive due to weak exchange force. Such spatial switching from repulsive to attractive interaction between inter-layer excitons in the moiré superlattice opens an avenue for tunable interaction.

To achieve enhanced interaction among moiré excitons in an experimental framework, we need to meet two important criteria: (a) a larger twist angle that helps in reducing both the size of the moiré well and the inter-moiré well separation - simultaneously enhancing intra- and inter-moiré well Coulomb interaction [10, 11] (see Figure 1c); and (b) a large fill factor that drives such inter-excitonic interaction. Unfortunately, it is challenging to meet both criteria simultaneously in an experimental setup since one must have a large excitation density to achieve a fill factor > 1 in a sample with dense moiré pockets. The large optical power required to achieve such high excitation density causes spectral broadening of the moiré trapped ILE emission peaks, smearing out the key spectroscopic signatures of inter-excitonic interactions. This necessitates a novel moiré sample design, as discussed below.

We fabricate twisted WS_2/WSe_2 hetero-bilayer samples on polymer nanopillar (height: 100 nm, diameter: 150 nm) patterned on a gold film, as shown in Figure 2a (see details of the sample fabrication in **Methods**). Figure 2b shows a schematic of the cross-section of the structure with a cross-sectional scanning electron micrograph (SEM) in the inset. We keep a relatively large twist angle ($>5^\circ$) between the two monolayers, facilitating intra- and inter-moiré well Coulomb interaction.

The pillar structure has several advantages over flat samples: The local strain produced by the nanopillar reduces the bandgap at the top of the pillar, allowing an optically-generated ILE to funnel to the pillar site [12–14] (Figure 2b,c). This helps us achieve a large fill factor locally at the top of the nanopillar without the need for applying a large optical power.

The underneath gold film quenches the exciton emission away from the pillar site due to non-

radiative exciton transfer to gold, thus allowing us to selectively collect the photons from the top of the pillar [15, 16]. Figure 2d shows the spatial intensity map of second harmonic generation (SHG) and exciton photoluminescence (PL) signal (in the inset, around the marked pillar) of a representative sample with a twist angle of $\sim 6^\circ$ (confirmed by polarization-resolved SHG polar plot in Supporting Information 1. Both maps indicate that the measured intensity is the maximum on the pillars and is significantly suppressed on gold.

The enhanced SHG signal on the pillar with respect to the flat part on gold arises due to a combination of (1) the incident laser’s electric field having an antinode near the gold surface and (2) strain on top of the nanopillar [17–19]. More details are discussed in Supporting Information 2. Both far-field radiation pattern of the SHG signal and the angular distribution of the SHG polarization suggest that the strain on the pillar does not introduce any anisotropy (see Supporting Information 3 for details).

In the case of PL, the enhancement on the nanopillar compared to the flat regions of monolayers touching gold is due to exciton funneling to the pillar site and quenching of excitons away from the pillar. Quenching of excitons away from the pillar is due to multiple reasons, such as, (1) the non-radiative loss of excitons to gold from the flat regions [15, 16], (2) excitation laser field having an antinode on the gold surface (see Supporting Information 2), and (3) reduced far-field component of the emission (see Supporting Information 4). This allows us to collect ILE emission from a much smaller ensemble of moiré wells on the pillar compared to a flat sample, the collection area in the latter case being limited by the diffraction-limited laser spot. This dramatically reduces the inhomogeneous broadening of the ILE emission peaks, helping us resolve interaction-driven, closely spaced peaks. Figure 2e compares the typical emission spectra from a pillar sample and a hBN-capped flat sample. ILE peaks from the pillar sample exhibit a full-width at half-maximum (fwhm) of ~ 6 meV - which is a 5-fold reduction compared with flat samples. See Supporting Information 5 for emission spectrum from another pillar sample with fwhm of 4.9 meV, while the corresponding flat portion on gold of the same sample shows a weak emission peak with fwhm of ~ 34 meV.

Further, the gold film also acts as a back reflector, reducing the loss of photons emitted in the downward direction (see Figure 2f for emission pattern). Note that the pillars are made of photoresist polymer with a low dielectric constant of 2.62. Further, we avoid capping the sample with hBN to reduce dielectric screening. This low dielectric environment maintains a high degree of Coulomb interaction among the excitons.

As reported previously [12, 14, 20, 21], the conduction band of WS_2 is tunable with strain, whereas the valence band of WSe_2 does not change appreciably (left panel of Figure 2c). The strain thus effectively reduces the local band gap and, consequently, the ILE emission energy, as shown in the right panel of Figure 2c. In addition, strain induced selective lowering of the conduction band gives rise to an inward electron flux towards the top of the pillar [22, 23], which leads to a possibility of electron doping at the pillar site.

In the rest of the paper, we focus on a sample (with data from additional samples discussed in Supporting Information 6 and Supporting Information 8) whose integrated PL emission map at 300 K is shown in Figure 3. The dashed line demarcates the hetero-bilayer region from the WSe_2 monolayer. In both regions, an array of brightly emitting nanopillars is visible, surrounded by a dark background, as expected from the earlier discussion. To estimate the strain-induced bandgap reduction quantitatively, Figure 3b presents spatial maps of the PL intensity, integrated over different energy ranges as indicated. Each spatial point is normalized by the total spectral emission at that point. Data for monolayer, hetero-bilayer, one of the monolayer covered pillars (black circles in Figure 3b), and one of the hetero-bilayer covered pillars (blue circles in Figure 3b) are picked from the map and plotted in Figure 3c for better visualization. The monolayer WSe_2 portion is the brightest around 1.655 eV, corresponding to the excitonic energy of the monolayer. Note that both the hetero-bilayer portion and the pillars are dark for this range and are brighter in lower energy maps, suggesting a red shift for both of these regions (Figure 3b). The flat hetero-bilayer portion becomes the brightest at 1.635 eV (Figure 3c) and is thus 20 meV red-shifted compared to the flat monolayer portion. Monolayer-covered pillars exhibit a maximum emission around 1.605 eV, giving a strain-induced redshift of 50 meV compared to the flat monolayer portion. Similarly, the hetero-bilayer-covered pillars

show maximum emission at 1.595 eV, giving a strain-induced redshift of 40 meV compared to the flat hetero-bilayer portion.

Figure 4 summarizes the key experimental findings of this work. Figure 4a shows the PL intensity at a pillar site at 5 K in a color plot as a function of the incident power (P) of a 532 nm laser and the emission photon energy. The line-cuts at three different P values are shown in Figure 4b. In Figure 4c, we show the variation of the intensity (I) of different ILE peaks as a function of P , and fit them using a power law ($I \propto P^\gamma$). The corresponding transitions between states are summarized in Figure 4d.

We look for the peaks that are discernible at the lowest P (bottom panel of Figure 4b) and assign them as the neutral exciton (X_0 and X_1) resonances arising from the ground state and first excited state of the moiré potential well. Surprisingly, we observe a strong nonlinearity with $\gamma = 1.78 \pm 0.25$ for X_0 (fwhm = 5.4 meV) for nearly a 10-fold change in P (Figure 4c). Data from another sample exhibiting superlinearity of X_0 is given in Supporting Information 6. X_1 also exhibits superlinearity with P , however, with a reduced degree ($\gamma = 1.27 \pm 0.11$, see Supporting Information 7). This is a stark anomaly from conventional neutral exciton power law with $\gamma \approx 1$ for free excitons [3, 5, 24, 25] and $\gamma \leq 1$ for trapped excitons [5, 15, 26, 27]. As discussed below, such a superlinear power law is a signature of inter-moiré well repulsive dipolar interaction.

The Coulomb interaction operator between two inter-layer excitons is given by

$$\hat{V}_{int} = V(\mathbf{r}_{e1} - \mathbf{r}_{e2}) + V(\mathbf{r}_{h1} - \mathbf{r}_{h2}) - V'(\mathbf{r}_{e1} - \mathbf{r}_{h2}) - V'(\mathbf{r}_{e2} - \mathbf{r}_{h1}) \quad (1)$$

where,

$$V = \frac{e^2}{\epsilon r} \quad \text{and} \quad V' = \frac{e^2}{\epsilon \sqrt{r^2 + d^2}} \quad (2)$$

e is the electronic charge, ϵ is the effective dielectric constant, d is the inter-layer separation, and r is the absolute of the in-plane relative coordinate. The presence of both positive and negative terms gives rise to a complex competition between direct and exchange terms. However,

when the excitons are trapped in the neighboring moiré wells, the potential barrier in between results in negligible wave function overlap, suppressing the exchange interaction. Thus, in this inter-moiré well interaction scenario, the direct Coulomb term dominates, and the inter-layer excitons create a repulsive environment for others trapped in the neighboring moiré wells.

To understand the superlinearity from such repulsive interaction, we calculate the exciton density $n(x, t)$ at a radial distance x from the center of the strain well (see **Methods** for derivation):

$$\frac{\partial n(x, t)}{\partial t} = -\frac{\partial F(x)}{\partial x} + g(x) - \frac{n(x)}{\tau_e} - \lambda n^2(x) \quad (3)$$

The first term on the right-hand side represents the gradient of the total exciton flux (F), which incorporates three key processes: the outward flux of excitons due to (a) concentration gradient and (b) exciton-exciton dipolar repulsion; and their inward drift driven by (c) a strain gradient. The generation rate of excitons, $g(x)$, follows a Gaussian spatial distribution and scales with P . The parameter τ_e is the effective exciton lifetime, encompassing radiative and non-radiative decay mechanisms apart from the Auger process, while λ represents the Auger annihilation coefficient. Solving for the steady-state condition ($\frac{\partial n(x, t)}{\partial t} = 0$), $n(x)$ is determined numerically and is shown in Figure 5a (bottom panel) for different values of P . At lower P , $n(x)$ peaks at the nanopillar center due to exciton funneling caused by strain. This results in the trapping of excitons within moiré pockets at the lowest energy point of the strain-induced potential (Figure 5a, top panel). As P increases, repulsive dipolar interaction between excitons in adjacent moiré pockets becomes significant, raising the exciton energy with their density [5, 6, 28]. This elevates the local exciton energy at the center of the nanopillar where the exciton density is maximum, partially offsetting the strain-induced energy lowering. Consequently, the overall energy profile starts to flatten at the center of the nanopillar. The size of this flattened region increases with P . The flattening of the energy well gives rise to an increasing number of equipotential moiré pockets available for filling (Figure 5a, top panel). This increasing number of emitting moiré pockets gives rise to the superlinearity observed in our sample. When the size of the energetically flat region crosses the size of the strain well, the newer moiré pockets being filled reside on the metal substrate. These contribute little to the overall emission due to non-radiative charge transfer to gold. This limit, combined with the saturation of the individual

moiré pocket emission [given by $I = I_{\text{max}} \cdot P/(P + P_{\text{sat}})$] [26, 29, 30], leads to the saturation of emission intensity at higher P . We overlay the experimental data with emission intensity calculated from the model (Figure 5b) and are able to fit both the initial superlinear increase, followed by the saturating behavior. The observations suggest an optically-driven dynamic tuning of the strain well size and, in turn, effective pillar diameter.

With an increase in P , new emission peaks appear on both lower and higher energy sides of X_0 . On the lower energy side, we observe a trion (X_0^-), about 4.5 meV below the X_0 peak - in good agreement with previously reported moiré trions [31, 32]. The X_0^- peak can be characterized with a $\gamma = 1.34 \pm 0.05$ (Figure 4c, middle panel). The appearance of X_0^- with an increase in P is due to the photoinduced doping that results from the additional photoelectrons funneling towards the pillar site due to the strain induced curvature of the conduction band edge (left panel of Figure 2c) [20, 33]. Note that the spectral location of X_0 does not change appreciably over a wide range of power - an observation that is made in all our samples. This indicates that with an increase in P , the photo-electron doping induced red shift [5] likely compensates for the dipolar repulsion driven blue shift.

At higher P , we observe an intense peak (XX_{00}) below X_0^- . XX_{00} exhibits a power law index of 3.02 ± 0.48 (1.68 ± 0.12) with respect to P (X_0) (Figure 4c, bottom panel). Such strong superlinearity with respect to X_0 indicates the biexcitonic origin of the peak that results from the radiative transition $XX_{00} \rightarrow X_0$ (see Figure 4d). The corresponding emission energy $\hbar\omega(XX_{00})$ being energetically lower than the X_0 resonance clearly suggests a negative binding energy (~ 11 meV), leading to a stabilization of the biexciton inside a moiré well when local fill factor is more than unity. Results from another sample are shown in Supporting Information 8, clearly exhibiting prominent X_0 , X_0^- , and XX_{00} emission peaks. Note that such a scenario of biexciton stabilization is distinct from previous works demonstrating two excitons forcefully confined by the moiré potential well, which would otherwise be unbounded [8, 9].

To understand the origin of such intra-moiré attractive interaction, we use variational calculations (see **Methods** for details) to estimate the binding energy of the biexciton. We construct

the spatial part of the singlet (triplet) form [indicated by the upper (lower) sign] of the total wave function of the two-exciton state, maintaining symmetry (anti-symmetry) under the exchange of position of either electron or hole:

$$\begin{aligned}\Psi^\pm(\mathbf{r}_{e1}, \mathbf{r}_{h1}, \mathbf{r}_{e2}, \mathbf{r}_{h2}) &\propto \psi(\mathbf{r}_{e1}, \mathbf{r}_{h1})\phi(\mathbf{r}_{e2}, \mathbf{r}_{h2}) \pm \psi(\mathbf{r}_{e2}, \mathbf{r}_{h1})\phi(\mathbf{r}_{e1}, \mathbf{r}_{h2}) \\ &\quad \pm \psi(\mathbf{r}_{e1}, \mathbf{r}_{h2})\phi(\mathbf{r}_{e2}, \mathbf{r}_{h1}) + \psi(\mathbf{r}_{e2}, \mathbf{r}_{h2})\phi(\mathbf{r}_{e1}, \mathbf{r}_{h1})\end{aligned}\quad (4)$$

Here ψ and ϕ denote the two individual exciton wave functions (parameterized by inter-exciton separation ρ and width of exciton wave packet ζ , see **Methods**) with corresponding electron (hole) coordinates denoted by $\mathbf{r}_{e(h)i}$ for the i^{th} exciton. With \hat{H} being the total Hamiltonian, we obtain the energy of the biexciton state as

$$\begin{aligned}U^\pm(\rho, \zeta) &= \langle \Psi^\pm(\mathbf{r}_{e1}, \mathbf{r}_{h1}, \mathbf{r}_{e2}, \mathbf{r}_{h2}) | \hat{H} | \Psi^\pm(\mathbf{r}_{e1}, \mathbf{r}_{h1}, \mathbf{r}_{e2}, \mathbf{r}_{h2}) \rangle \\ &= \int d\mathbf{r}_{e1} d\mathbf{r}_{h1} d\mathbf{r}_{e2} d\mathbf{r}_{h2} \Psi^{\pm*}(\mathbf{r}_{e1}, \mathbf{r}_{h1}, \mathbf{r}_{e2}, \mathbf{r}_{h2}) \hat{H} \Psi^\pm(\mathbf{r}_{e1}, \mathbf{r}_{h1}, \mathbf{r}_{e2}, \mathbf{r}_{h2})\end{aligned}\quad (5)$$

For large ρ , the inter-exciton interaction becomes negligible, and thus $U^\pm \rightarrow 2E_{X_0}$. Therefore, the binding energy of the singlet (upper sign) and triplet (lower sign) biexciton can be estimated for a given ρ and ζ as

$$E_b^\pm = [\lim_{\rho \rightarrow \infty} U^\pm(\rho, \zeta_0)] - U^\pm(\rho, \zeta) \quad (6)$$

where ζ_0 is the width of a single exciton wave packet, in the absence of any interaction with the other exciton.

In Figure 1d, we plot the triplet biexciton binding energy as a function of the variational parameters ζ and ρ . Three line-cuts at different ζ are shown in Figure 1e. Large ζ represents excitons that are not trapped inside a moiré pocket. From the repulsive nature of the interaction potential (Equation 1), we expect the triplet state to have lower energy than the singlet state, as evidenced by the plot in Figure 1f. Interestingly, the calculations indicate that the energy minimum of the triplet state occurs for a length scale where two excitons are inside a single moiré well in our samples, suggesting that it is possible to achieve a stabilization of the biexciton state with $E_b < 0$, thanks to the strong exchange interaction.

Note that, the calculations suggest that the biexciton formation leads to the pulling of the two constituent excitons close to the center of the moiré pocket (although, they do not exactly collapse to the center as the repulsion eventually starts dominating, as depicted in the bottom left corner of Figure 1d). This, in turn, creates a strong wave function overlap between XX_{00} and X_0 , creating a high radiative decay rate for the $XX_{00} \rightarrow X_0$ transition. On the other hand, as pointed out recently [9], had the two excitons experienced a net repulsive interaction, they would be pushed towards the opposite edges of the moiré pocket. This would reduce the wave function overlap between the initial XX_{00} state and the final X_0 state during the radiative transition, suppressing XX_{00} luminescence. Thus, the experimental observation of strong photoluminescence intensity from the XX_{00} peak in our sample is a signature of the attractive intra-moiré excitonic interaction.

Further, the time-resolved photoluminescence (TRPL) measurement of X_0 and XX_{00} (see Supporting Information 9) provides additional signature of moiré biexciton formation. We observe a non-monoexponential decay for both the species, coupled with a delayed luminescence from the biexciton with respect to the exciton, suggesting biexciton formation from excitons. Both these results are in good agreement with our model that incorporates coupled nonlinear differential equations describing the dynamics of X_0 and XX_{00} (see Supporting Information 9). In addition, we also observe a fast initial decay (< 100 ps) for the exciton, unlike flat samples [5, 34], suggesting a fast conversion channel of exciton to biexciton, especially at higher exciton density.

At high P , more peaks appear (shaded in orange and green in Figure 4b) in the emission spectrum with superlinear power law - indicative of multi-particle excitonic states. Further investigation is necessary to assign the specific origin of these peaks. The orange peak around 1.45 eV is particularly interesting, with $\gamma = 1.68 \pm 0.19$ (see Supporting Information 7). We assign this state as the biexciton (XX_{01}) formed from the excitons at X_0 and X_1 states. There are two recombination pathways of the XX_{01} , namely, (a) $XX_{01} \rightarrow X_0$ (higher emission energy) and (b) $XX_{01} \rightarrow X_1$ (lower emission energy, see Figure 4d). The former corresponds to the orange shaded peak. A similar separation among the pairs $X_0 - XX_{00}$ and $X_1 - XX_{01}$ suggests

similar binding energy of XX_{00} and XX_{01} . This also indicates that the photons emitted from the latter transition are energetically close to the $XX_{00} \rightarrow X_0$ emission and hence are likely spectrally masked by the bright XX_{00} emission.

To conclude, using a strained hetero-bilayer on a nanopillar, we demonstrate that the exchange force can overcome repulsive interaction between two inter-layer excitons and form a stable triplet biexciton inside a single moiré well. This could lead to possible many-body explorations such as the formation of droplets of moiré excitons and interaction among droplets trapped in individual moiré pockets.

Methods

Variational method to estimate the stability of biexciton

We start with considering the wave function of the individual moiré excitons exhibiting Gaussian wave packet with an s-state like structure [8]. We take two exciton wave packets which are symmetrically positioned around the center of the moiré well, and the corresponding wave functions are of the form $\psi = Ke^{-\frac{(R-\rho/2)^2}{2\zeta^2}}e^{-\frac{r}{a_0}}$ and $\phi = Ke^{-\frac{(R+\rho/2)^2}{2\zeta^2}}e^{-\frac{r}{a_0}}$, where $\mathbf{R} = \frac{\mathbf{r}_e + \mathbf{r}_h}{2}$ and $\mathbf{r} = \frac{\mathbf{r}_e - \mathbf{r}_h}{2}$, ζ is the width of the Gaussian wave packet, a_0 is the Bohr radius of the exciton, ρ is the separation between the two excitons along the radial direction of the moiré well, and K is a normalization constant. Such a simplified form of the wave function may not necessarily obey the complex symmetry of a moiré well after relaxation, especially in the presence of local inhomogeneity. However, this is good enough to elucidate the essential physics required to understand the binding of the excitons within a moiré well, particularly at slightly larger twist angles (as is the case in this work). For single exciton, we assume $a_0 = 2$ nm, and $\zeta \equiv \zeta_0 = 2$ nm [8]. \mathbf{r}_e and \mathbf{r}_h are the electron and hole spatial coordinates. We assume that the Bohr radius of individual exciton remains unchanged during exciton-exciton interaction. We construct the spatial part of the singlet (triplet) form [indicated by the upper (lower) sign] of the total wave function of the two-exciton state, maintaining symmetry (anti-symmetry) under the exchange

of position of either electron or hole:

$$\begin{aligned}\Psi^\pm(\mathbf{r}_{e1}, \mathbf{r}_{h1}, \mathbf{r}_{e2}, \mathbf{r}_{h2}) = & K_0[\psi(\mathbf{r}_{e1}, \mathbf{r}_{h1})\phi(\mathbf{r}_{e2}, \mathbf{r}_{h2}) \pm \psi(\mathbf{r}_{e2}, \mathbf{r}_{h1})\phi(\mathbf{r}_{e1}, \mathbf{r}_{h2}) \\ & \pm \psi(\mathbf{r}_{e1}, \mathbf{r}_{h2})\phi(\mathbf{r}_{e2}, \mathbf{r}_{h1}) + \psi(\mathbf{r}_{e2}, \mathbf{r}_{h2})\phi(\mathbf{r}_{e1}, \mathbf{r}_{h1})]\end{aligned}\quad (7)$$

where K_0 is the normalization constant, and the corresponding electron (hole) coordinates are denoted by $\mathbf{r}_{e(h)i}$ for the i^{th} exciton.

With this construction, we ensure that:

For exciton exchange ($\mathbf{r}_{e1} \leftrightarrow \mathbf{r}_{e2}$ and $\mathbf{r}_{h1} \leftrightarrow \mathbf{r}_{h2}$): $\Psi^\pm \rightarrow \Psi^\pm$

For electron exchange ($\mathbf{r}_{e1} \leftrightarrow \mathbf{r}_{e2}$): $\Psi^\pm \rightarrow \pm\Psi^\pm$

For hole exchange ($\mathbf{r}_{h1} \leftrightarrow \mathbf{r}_{h2}$): $\Psi^\pm \rightarrow \pm\Psi^\pm$

Now, the total Coulomb potential operator is given by:

$$\begin{aligned}\hat{V} = & V(\mathbf{r}_{e1} - \mathbf{r}_{e2}) + V(\mathbf{r}_{h1} - \mathbf{r}_{h2}) - V'(\mathbf{r}_{e1} - \mathbf{r}_{h1}) - V'(\mathbf{r}_{e2} - \mathbf{r}_{h2}) \\ & - V'(\mathbf{r}_{e1} - \mathbf{r}_{h2}) - V'(\mathbf{r}_{e2} - \mathbf{r}_{h1})\end{aligned}\quad (8)$$

where,

$$V(\mathbf{r}) = \frac{e^2}{\epsilon r} \quad \text{and} \quad V'(\mathbf{r}) = \frac{e^2}{\epsilon\sqrt{r^2 + d^2}}\quad (9)$$

The full Hamiltonian, including the kinetic energy terms for all four particles, is then

$$\hat{H} = -\frac{\hbar^2}{2m_e}\nabla^2_{\mathbf{r}_{e1}} - \frac{\hbar^2}{2m_e}\nabla^2_{\mathbf{r}_{e2}} - \frac{\hbar^2}{2m_h}\nabla^2_{\mathbf{r}_{h1}} - \frac{\hbar^2}{2m_h}\nabla^2_{\mathbf{r}_{h2}} + \hat{V}\quad (10)$$

The energy of the four particle system is then:

$$\begin{aligned}U^\pm(\rho, \zeta) = & \langle \Psi^\pm(\mathbf{r}_{e1}, \mathbf{r}_{h1}, \mathbf{r}_{e2}, \mathbf{r}_{h2}) | \hat{H} | \Psi^\pm(\mathbf{r}_{e1}, \mathbf{r}_{h1}, \mathbf{r}_{e2}, \mathbf{r}_{h2}) \rangle \\ = & \int d\mathbf{r}_{e1} d\mathbf{r}_{h1} d\mathbf{r}_{e2} d\mathbf{r}_{h2} \Psi^{\pm*}(\mathbf{r}_{e1}, \mathbf{r}_{h1}, \mathbf{r}_{e2}, \mathbf{r}_{h2}) \hat{H} \Psi^\pm(\mathbf{r}_{e1}, \mathbf{r}_{h1}, \mathbf{r}_{e2}, \mathbf{r}_{h2})\end{aligned}\quad (11)$$

For large ρ , the inter-exciton interaction becomes negligible, and thus $U^\pm \rightarrow 2E_X$. There-

fore, the binding energy of the biexciton can be estimated for a given ρ and ζ as

$$E_b^\pm = [\lim_{\rho \rightarrow \infty} U^\pm(\rho, \zeta_0)] - U^\pm(\rho, \zeta) \quad (12)$$

We vary ρ and ζ as variational parameters. We plot E_b in Figure 1d as a function of ρ and ζ , and look for the minimum of E_b . For calculations, we have assumed $d = 0.6$ nm and $\epsilon = 6.5\epsilon_0$, where ϵ_0 is the permittivity of vacuum. The stability of the biexciton is analyzed in Supporting Information 10 for different values of d and ϵ . Further, in Supporting Information 11, we show the role of twist angle (and hence, moiré well size) on the stability of the biexciton.

Numerical solution of combined drift-diffusion equation

Nanopillars introduce a non-uniform strain on the TMD monolayer, which can be considered parabolic with its maximum in the center of the nanopillar. The band gap reduction can thus be modelled as a parabolic function with its minimum at the center of the nanopillar. The energy of the ILE (E_{ILE}) in the presence of such parabolic strain can be written as:

$$E_{ILE} = E_g - \frac{1}{2}kx^2 \quad (13)$$

Here k quantifies the relation between the magnitude of strain and the band gap reduction, E_g is the inter-layer bandgap for a flat sample, and x is the radial distance from the center of the pillar. Dipole-dipole repulsion can be taken into account by addition of the term $\alpha_{dd}n(x)$ where α_{dd} is the strength of dipole-dipole repulsion and $n(x)$ is the ILE density in the system [5, 6, 28]. The overall energy of the ILE in the system is then given by:

$$E_{ILE} = E_g - \frac{1}{2}kx^2 + \alpha_{dd}n(x) \quad (14)$$

There will be a drift of ILE due to this non-uniform band gap, which can be modeled as a drift under an induced electric field given by:

$$E_F(x) = \frac{-1}{e} \frac{\partial E_{ILE}}{\partial x} \quad (15)$$

Taking into account the diffusion of ILE to get the total flux (F) of excitons at a particular

point in the system:

$$F = \mu_e n E_F - D_e \frac{\partial n}{\partial x} \quad (16)$$

μ_e and D_e are the drift mobility and diffusion constant for excitons, respectively.

Considering other factors, such as the radiative or nonradiative decay of ILE (overall lifetime τ_e), Auger annihilation (rate constant λ), and the generation rate from optical pumping [$g(x)$], the rate of change of ILE density in space and time is thus given by the following rate equation:

$$\frac{\partial n(x)}{\partial t} = -\frac{\partial F}{\partial x} + g(x) - \frac{n(x)}{\tau_e} - \lambda n^2(x) \quad (17)$$

Values of μ_e , D_e , and λ are taken from literature [35–37].

Sample fabrication

A 30/40 nm thick Ti/Au layer is deposited onto a Si substrate (coated with 285 nm thick thermally grown SiO₂) using a sputtering process. A layer of negative tone resist (ma-N-2403 from micro resist technology) is spin-coated on the substrate. The resist is then cured by heating the substrate at 90°C for 2 minutes. A pattern of solid circles is defined on the resist-coated substrate through electron beam lithography, with an accelerating voltage of 30 kV and a 10 μ m aperture. The circles in the pattern have a diameter of 150 nm, arranged in an array with a spacing of 5 μ m (which is well beyond our laser spot size so that, at a time, only one pillar is excited by the laser during measurement). The electron beam selectively hardens the resist in the areas corresponding to the circular pattern. Following this, the substrate is developed using AZ-726 MIF developer to remove the unexposed resist. To enhance the mechanical durability of the nanopillars, the substrate undergoes a hard-bake process at 150°C for 15 minutes, preparing it for subsequent layer transfer steps.

Both WSe₂ and WS₂ layers are exfoliated on separate polydimethylsiloxane (PDMS) sheets, and appropriate monolayer flakes are identified under a microscope by optical contrast. We then use micro-manipulators to transfer these flakes one by one onto the patterned nanopillars. The entire structure is then annealed in vacuum (10^{-6} mbar) at 150°C for 3 hours.

Photoluminescence experiments

The PL measurements are carried out at 5 K temperature (unless otherwise stated) with a $\times 50$ objective (numerical aperture of 0.5). The excitation source used is a 532 nm laser operated in CW mode. The spot size for the laser is $\approx 1.5 \mu\text{m}$. PL spectra are recorded with a spectrometer consisting of a grating with 1800 lines per mm and CCD.

Far-field SHG intensity pattern imaging

The angular distribution of the SHG intensity from the sample was characterized using a back focal plane (BFP) imaging method. A 4f-lens imaging setup consists of a 180 mm tube lens followed by a 50 mm lens, which is used to project and map the back focal plane of the collection objective (20x/0.75 numerical aperture) onto a Peltier cooled Electron-Multiplying Charge-Coupled Device (EMCCD, iXon Ultra 897) detector plane. An appropriate shortpass (890 nm) and bandpass (520 ± 20 nm) filter are used to reject residual pump power and minimize background signal.

Author contributions

MC and SC contributed equally to this work. KM designed the experiment. MC and SC fabricated the samples and performed the measurements. PH and SA provided WSe₂ crystals for exfoliation. MC, SC and KM carried out the data analysis. SEM imaging was performed by SP. JKM, RB and VR performed the SHG measurements. MC and KM carried out the calculations. MC, SC and KM wrote the manuscript with input from all authors.

Data availability statement

Data available on reasonable request from the corresponding author.

Competing Interests

The authors declare no competing financial interest.

Acknowledgments

M.C. and K.M. acknowledge useful discussions with Varun Srivatsav Kondapally. This work was supported in part by National Quantum Mission, an initiative of the Department of Science and Technology (DST), Government of India, a Core Research Grant from the Science and Engineering Research Board (SERB) under DST, a grant from Indian Institute of Science under IoE, grants from Indian Space Research Organization (ISRO), a grant from DRDO, a grant under SERB TETRA, a grant from I-HUB QTF, IISER Pune, and a seed funding under Quantum Research Park (QuRP) from Karnataka Innovation and Technology Society (KITS), K-Tech, Government of Karnataka. S.A.T. acknowledges direct support from DOE-SC0020653 (excitonic testing of TMD crystals) and NSF CBET 2330110 (environmental testing of TMDs). SAT also acknowledges support from Applied Materials and Lawrence Semiconductors.

References

- [1] Gang Wang et al. “Colloquium: Excitons in Atomically Thin Transition Metal Dichalcogenides”. *Reviews of Modern Physics* 90.2 (2018), p. 021001.
- [2] Alexey Chernikov et al. “Exciton Binding Energy and Nonhydrogenic Rydberg Series in Monolayer WS_2 ”. *Physical Review Letters* 113.7 (2014), p. 076802.
- [3] Yumeng You et al. “Observation of Biexcitons in Monolayer WSe_2 ”. *Nature Physics* 11.6 (2015), p. 477.
- [4] Ziliang Ye et al. “Efficient Generation of Neutral and Charged Biexcitons in Encapsulated WSe_2 Monolayers”. *Nature Communications* 9.1 (2018), p. 3718.
- [5] Suman Chatterjee et al. “Harmonic to Anharmonic Tuning of Moiré Potential Leading to Unconventional Stark Effect and Giant Dipolar Repulsion in WS_2/WSe_2 Heterobilayer”. *Nature Communications* 14.1 (2023), p. 4679.
- [6] B. Laikhtman and R. Rapaport. “Exciton Correlations in Coupled Quantum Wells and Their Luminescence Blue Shift”. *Physical Review B* 80.19 (2009), p. 195313.
- [7] Xueqian Sun et al. “Enhanced Interactions of Interlayer Excitons in Free-Standing Heterobilayers”. *Nature* 610.7932 (2022), p. 478.

- [8] Heonjoon Park et al. “Dipole Ladders with Large Hubbard Interaction in a Moiré Exciton Lattice”. *Nature Physics* 19.9 (2023), p. 1286.
- [9] Samuel Brem and Ermin Malic. “Optical Signatures of Moiré Trapped Biexcitons”. *2D Materials* 11.2 (2024), p. 025030.
- [10] Long Zhang et al. “Twist-Angle Dependence of Moiré Excitons in $\text{WS}_2/\text{MoSe}_2$ Heterobilayers”. *Nature Communications* 11.1 (2020), p. 5888.
- [11] Sara Shabani et al. “Deep Moiré Potentials in Twisted Transition Metal Dichalcogenide Bilayers”. *Nature Physics* 17.6 (2021), p. 720.
- [12] Priya Johari and Vivek B. Shenoy. “Tuning the Electronic Properties of Semiconducting Transition Metal Dichalcogenides by Applying Mechanical Strains”. *ACS Nano* 6.6 (2012), p. 5449.
- [13] Tingting Shen, Ashish V. Penumatcha, and Joerg Appenzeller. “Strain Engineering for Transition Metal Dichalcogenides Based Field Effect Transistors”. *ACS Nano* 10.4 (2016), p. 4712.
- [14] Matthew Brooks and Guido Burkard. “Theory of Strain-Induced Confinement in Transition Metal Dichalcogenide Monolayers”. *Physical Review B* 97.19 (2018), p. 1.
- [15] Mayank Chhaperwal et al. “Simultaneously Enhancing Brightness and Purity of WSe_2 Single Photon Emitter Using High-Aspect-Ratio Nanopillar Array on Metal”. *Nano Letters* 24.40 (2024), p. 12461.
- [16] Raghav Chaudhary, Varun Raghunathan, and Kausik Majumdar. “Origin of Selective Enhancement of Sharp Defect Emission Lines in Monolayer WSe_2 on Rough Metal Substrate”. *Journal of Applied Physics* 127.7 (2020).
- [17] Zhizi Guan et al. “Strain-Induced Giant Second-Order Susceptibility in Monolayer WSe_2 ”. *Physical Review B* 111.24 (2025), p. 245423.
- [18] Sudeep Puri et al. “Substrate Interference and Strain in the Second-Harmonic Generation from MoSe_2 Monolayers”. *Nano Letters* 24.41 (2024), p. 13061.
- [19] Sehwan Chang et al. “Enhancement of Second-Harmonic Generation in a 64° Stacked WSe_2/WS_2 Heterobilayer with Local Strain”. *Nanotechnology* 35.14 (2024), p. 145201.

- [20] Iris Niehues et al. “Strain Control of Exciton-Phonon Coupling in Atomically Thin Semiconductors”. *Nano Letters* 18.3 (2018), p. 1751.
- [21] Ji Feng et al. “Strain-Engineered Artificial Atom as a Broad-Spectrum Solar Energy Funnel”. *Nature Photonics* 6.12 (2012), p. 866.
- [22] Hyeonwoo Lee et al. “Drift-Dominant Exciton Funneling and Trion Conversion in 2D Semiconductors on the Nanogap”. *Science Advances* 8.5 (2022), p. 1.
- [23] Moshe G. Harats et al. “Dynamics and Efficient Conversion of Excitons to Trions in Non-Uniformly Strained Monolayer WS₂”. *Nature Photonics* 14.5 (2020), p. 324.
- [24] Suman Chatterjee et al. “Probing Biexciton in Monolayer WS₂ through Controlled Many-Body Interaction”. *2D Materials* 9.1 (2022), p. 015023.
- [25] Jiani Huang, Thang B. Hoang, and Maiken H. Mikkelsen. “Probing the Origin of Excitonic States in Monolayer WSe₂”. *Scientific Reports* 6 (February 2016), p. 1.
- [26] Yu-Ming He et al. “Single Quantum Emitters in Monolayer Semiconductors”. *Nature Nanotechnology* 10.6 (2015), p. 497.
- [27] Yuming He et al. “Cascaded Emission of Single Photons from the Biexciton in Monolayered WSe₂”. *Nature Communications* (2016).
- [28] Zhe Sun et al. “Excitonic Transport Driven by Repulsive Dipolar Interaction in a van Der Waals Heterostructure”. *Nature Photonics* 16.1 (2022), p. 79.
- [29] Santosh Kumar et al. “Strain-Induced Spatial and Spectral Isolation of Quantum Emitters in Mono- and Bilayer WSe₂”. *Nano Letters* (2015).
- [30] Philipp Tonndorf et al. “Single-Photon Emission from Localized Excitons in an Atomically Thin Semiconductor”. *Optica* 2.4 (2015), p. 347.
- [31] Erfu Liu et al. “Signatures of Moiré Trions in WSe₂/MoSe₂ Heterobilayers”. *Nature* 594.7861 (2021), p. 46.
- [32] Xi Wang et al. “Moiré Trions in MoSe₂/WSe₂ Heterobilayers”. *Nature Nanotechnology* 16.11 (2021), p. 1208.
- [33] Sujay B. Desai et al. “Strain-Induced Indirect to Direct Bandgap Transition in Multilayer WSe₂”. *Nano Letters* 14.8 (2014), p. 4592.

- [34] Junho Choi et al. “[Twist Angle-Dependent Interlayer Exciton Lifetimes in van Der Waals Heterostructures](#)”. *Physical Review Letters* 126.4 (2021), p. 047401.
- [35] F. Cadiz et al. “[Exciton Diffusion in WSe₂ Monolayers Embedded in a van Der Waals Heterostructure](#)”. *Applied Physics Letters* 112.15 (2018).
- [36] Florian Dirnberger et al. “[Quasi-1D Exciton Channels in Strain-Engineered 2D Materials](#)”. *Science Advances* 7.44 (2021).
- [37] Long Yuan and Libai Huang. “[Exciton Dynamics and Annihilation in WS₂ 2D Semiconductors](#)”. *Nanoscale* 7.16 (2015), p. 7402.

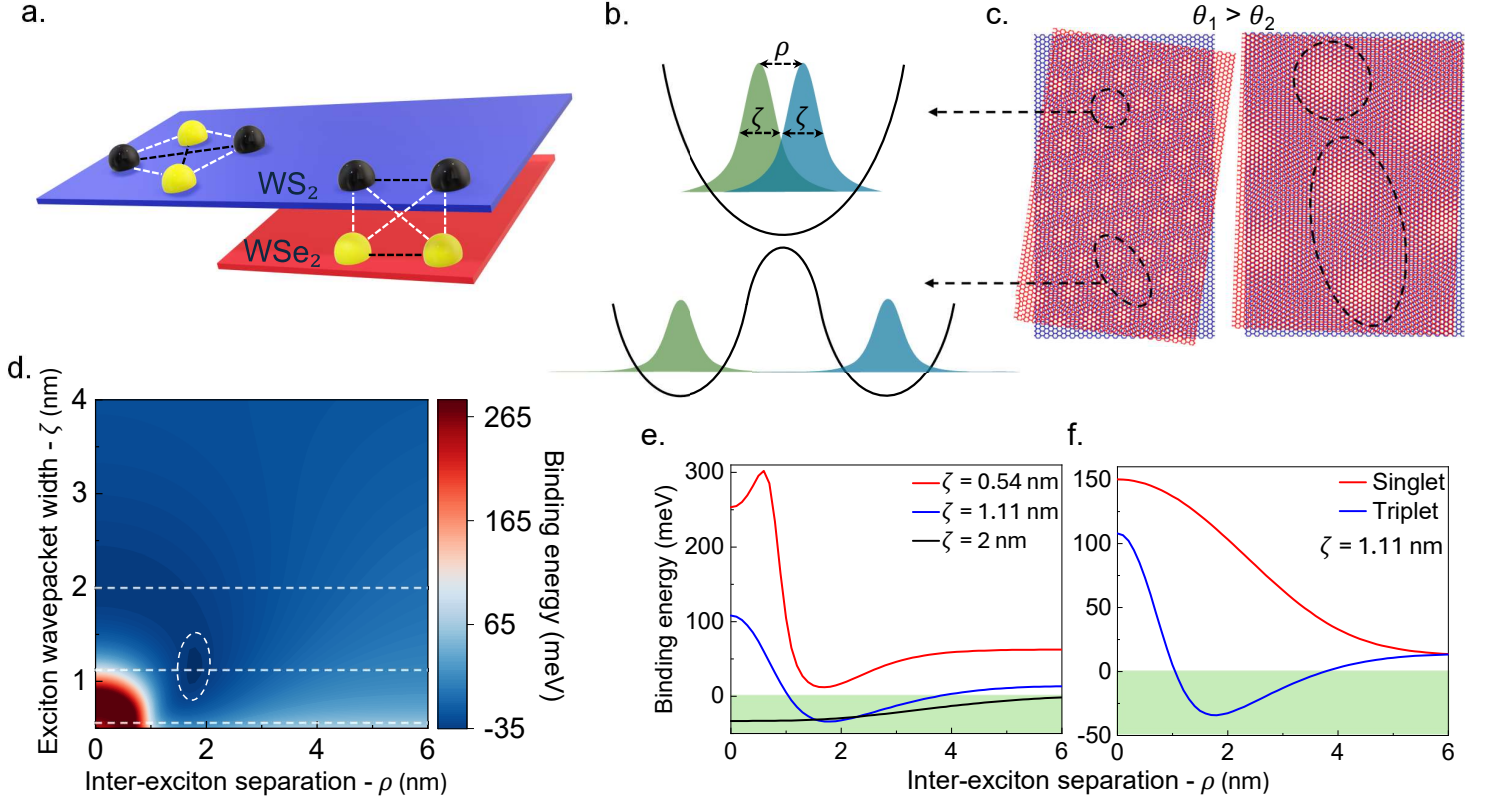


Figure 1: **Stabilization of moiré biexcitons:** (a) Schematic diagram showing electron (black spheres) and hole (yellow spheres) spatial arrangement for intra and inter-layer biexcitons in monolayer WS_2 and WS_2/WSe_2 heterojunction, respectively. In the latter case, electrons and holes are layer-polarized, which reduces the degrees of freedom for reconstruction. Black and yellow dashed lines indicate repulsion and attraction, respectively. (b) Schematic representation of two exciton wave packets (separation of ρ and width of ζ) trapped in the same (top panel) and neighboring (bottom panel) moiré well. (c) Moiré sample with a higher (left panel) and lower (right panel) twist angle, indicating the effect on moiré well size and inter-well separation. (d) A color plot showing the calculated binding energy of the triplet state of the biexciton inside a moiré well as a function of ρ and ζ . The white dashed circle indicates the most stable configuration having negative binding energy. (e) Line cuts along the dashed lines in (d). The green shaded region indicates stabilized biexciton regime. (f) Binding energy for singlet and triplet configuration for $\zeta = 1.11$ nm.

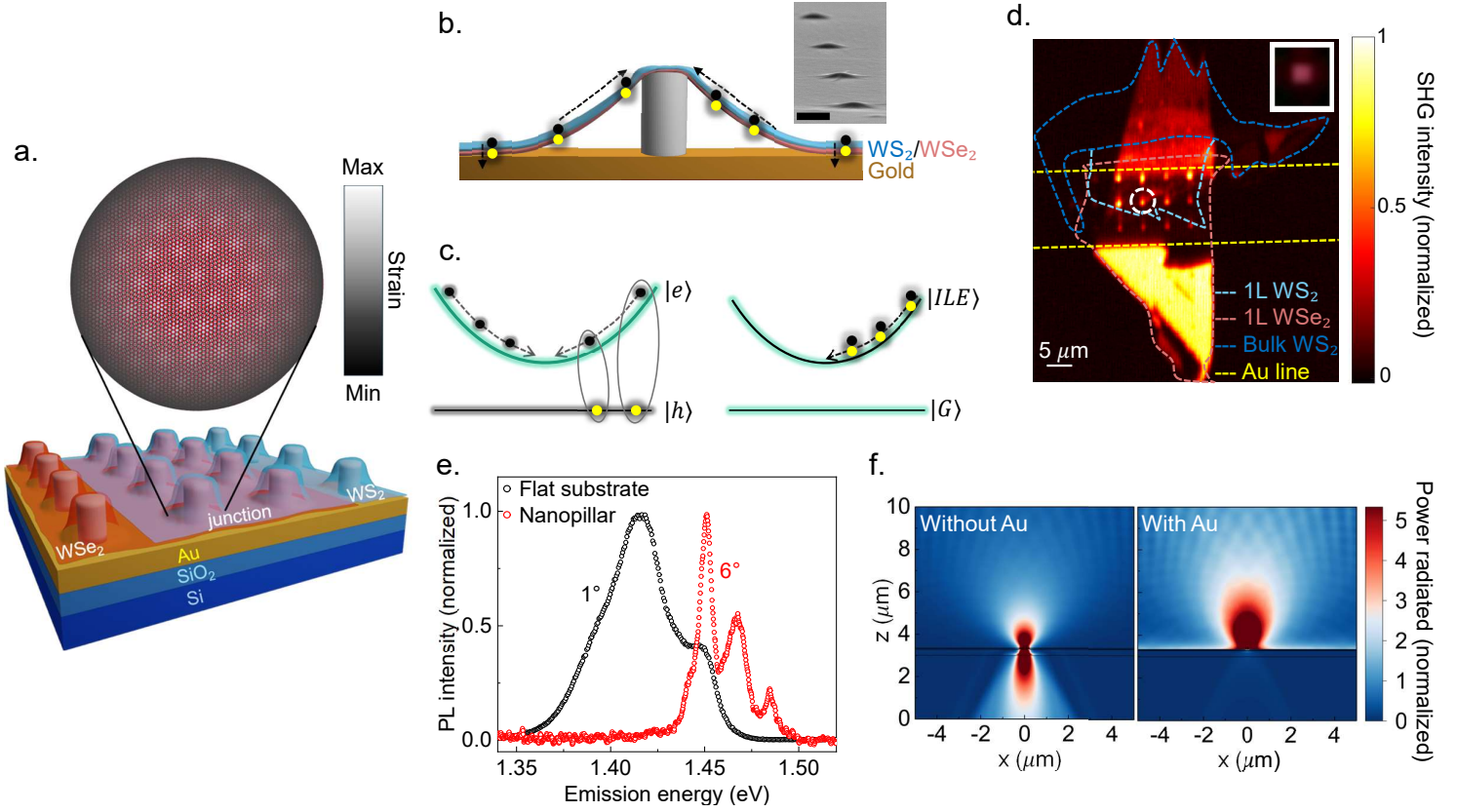


Figure 2: **Strained hetero-bilayer on nanopillar:** (a) Schematic representation of the strained WS_2/WSe_2 heterojunction on a periodic array of pillars with a gold film underneath. The zoomed-in view with a color bar schematically shows that the highest strain is applied on the pillar head (top panel). (b) Schematic cross-section of the structure. Arrows indicate strain-induced funneling of excitons towards the center of the pillar. On the flat portion, the ILE quenches due to nonradiative transfer to gold (downward arrow). The inset shows an SEM image of the hetero-bilayer on pillars. Scale bar: 500 nm. (c) Funneling (dragging) of electrons (holes) due to the formation of a bound ILE state. The conduction band bending due to strain is significant compared to the valence band. Left panel and right panel show the one-particle and two-particle pictures, respectively. (d) SHG map showing bright emission from pillar heads. Different layers are marked accordingly. Inset: PL map around the marked pillar indicating bright emission from the pillar surrounded by dark region. (e) PL emission spectra from flat (black symbols, twist angle $\sim 1^\circ$) and pillar (red symbols, twist angle $\sim 6^\circ$) samples at 5 K. (f) Simulation showing gold line acting as an efficient reflector to modify the ILE dipole radiation pattern.

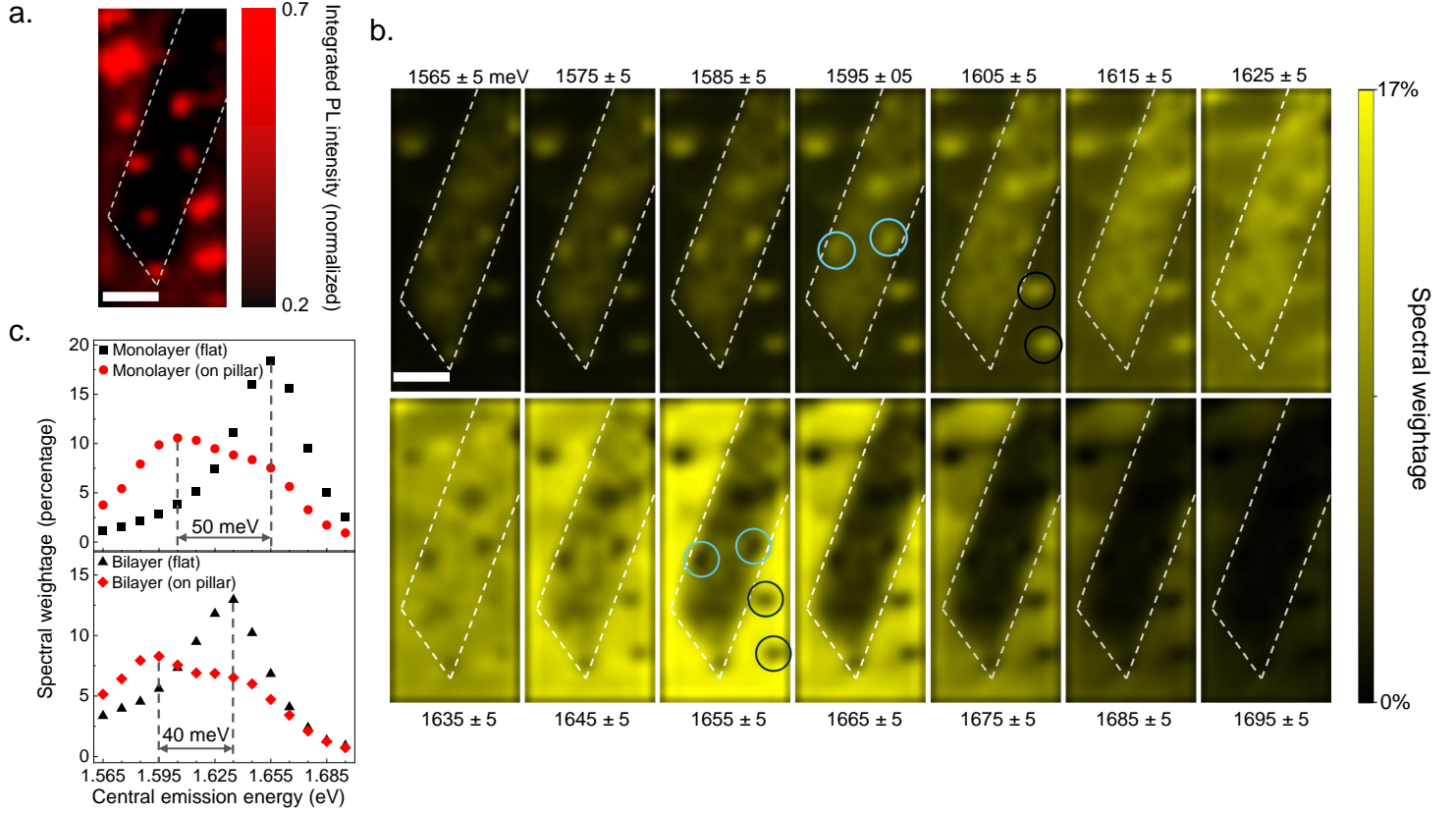


Figure 3: Quantitative estimation of strain induced bandgap reduction: (a) Integrated PL intensity map of the sample showing an array of brightly emitting pillars at 300 K. The white dashed line marks the hetero-bilayer region, and the remaining part is monolayer WSe₂. Scale bar: 5 μm (b) Spatial maps show the percentage of photons emitted within the energy ranges specified in each sub-figure (100% represents the total emission in the entire spectral range at a given spatial point). Black (blue) circles mark some selected pillars in the monolayer (hetero-bilayer) regions. Scale bar: 5 μm . (c) Spectral weightage for the flat monolayer, flat hetero-bilayer, one of the monolayer covered pillars (black circled), and one of the hetero-bilayer covered pillars (blue circled) is picked from the map in (b) and is plotted as a function of the corresponding energy range. The strain induced shift in emission energy of monolayer (hetero-bilayer) covered pillars with respect to flat monolayer (hetero-bilayer) portion is mentioned.

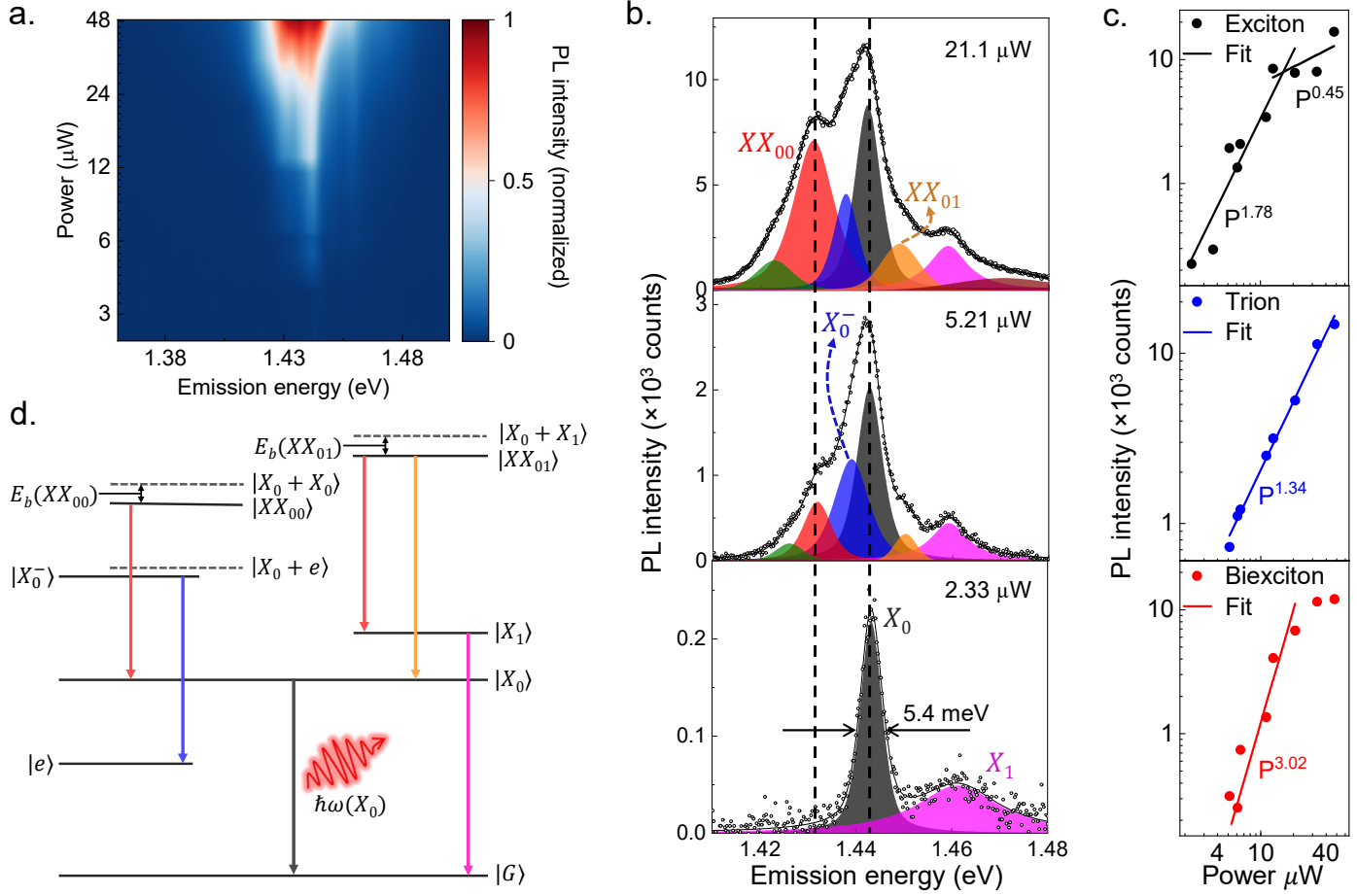


Figure 4: **Features of moiré exciton and biexciton emission on pillar:** (a) A color plot showing PL emission as a function of optical power and emission energy at 5 K. (b) Evolution of emission spectra with optical power showing fitted X_0 (black), X_1 (magenta), X_0^- (blue), XX_{00} (red), and XX_{01} (orange) peaks. The black dashed lines are a guide to the eye for X_0 and XX_{00} peaks. (c) Power law fitting of X_0 (top panel), X_0^- (middle panel), and XX_{00} (bottom panel) peaks. (d) Transition diagram showing radiative emission pathways of different states with the same color-coding as in (b).

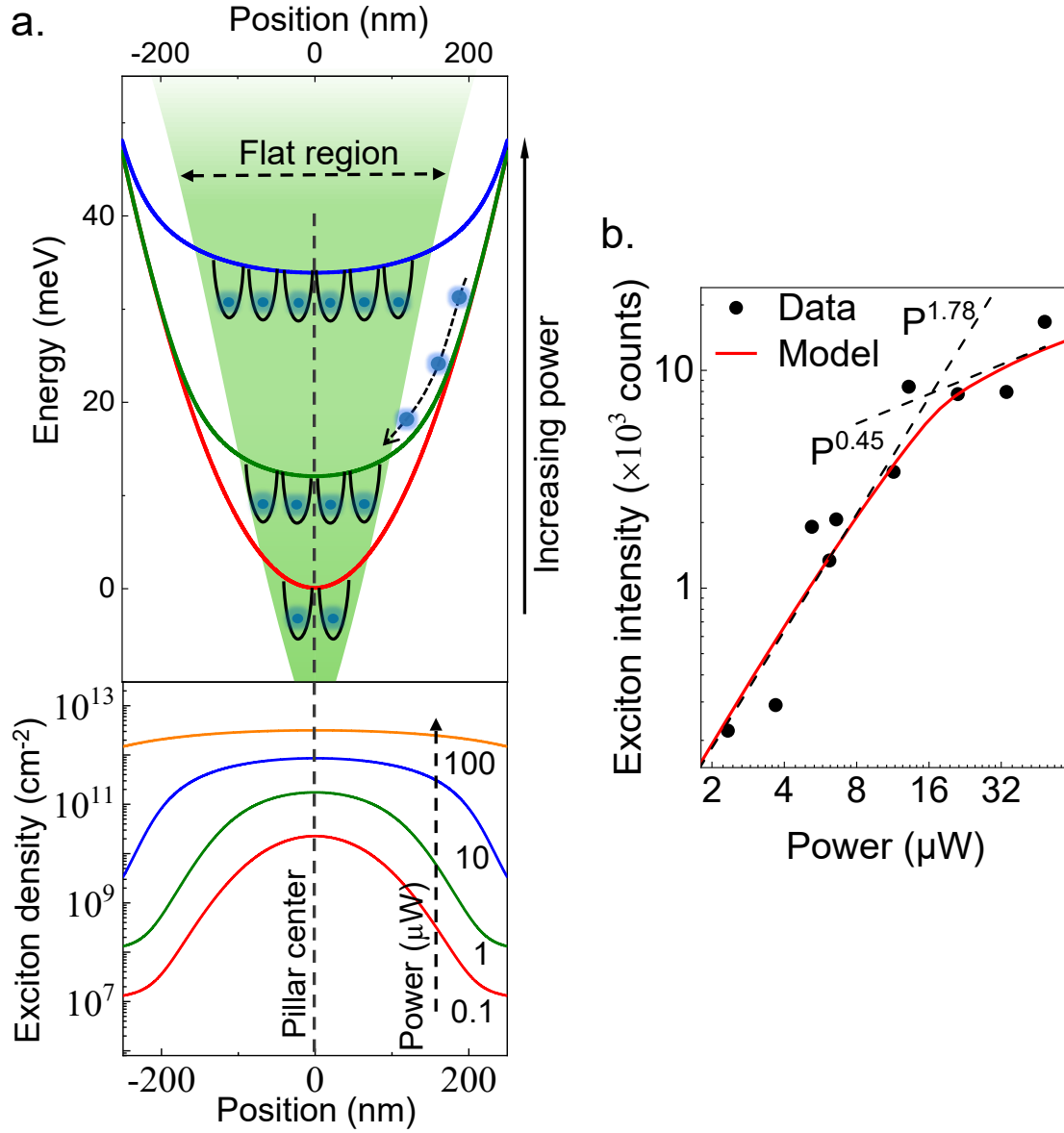


Figure 5: **Optical power dependent modulation of the strain well at pillar site:** (a) Top panel: The dipole-dipole repulsion gives rise to a flattening of the strain well profile, increasing the number of moiré wells filled with excitons. This gives rise to a superlinear power law in Figure 4c (top panel). Bottom panel: Calculated exciton density as a function of position from the pillar center at different power, suggesting flattening of the profile at higher power. (b) Emission intensity of X_0 as a function of power. Symbols indicate measured data, the dashed lines power law fitting, and the red trace shows the fitting from the model.

Supporting information for:

Observation of moiré trapped biexciton through
sub-diffraction-limit probing using hetero-bilayer on nanopillar

Mayank Chhaperwal^{1,||}, Suman Chatterjee^{1,2,||}, Suchithra Puliassery¹,
Jyothsna Konkada Manattayil¹, Rabindra Biswas^{1,3}, Patrick Hays⁴, Seth Ariel Tongay⁴,
Varun Raghunathan¹, and Kausik Majumdar^{1*}

¹Department of Electrical Communication Engineering,
Indian Institute of Science, Bangalore 560012, India

²Currently at Quantum Matter Institute, University of British Columbia,
Vancouver, British Columbia V6T 1Z4, Canada

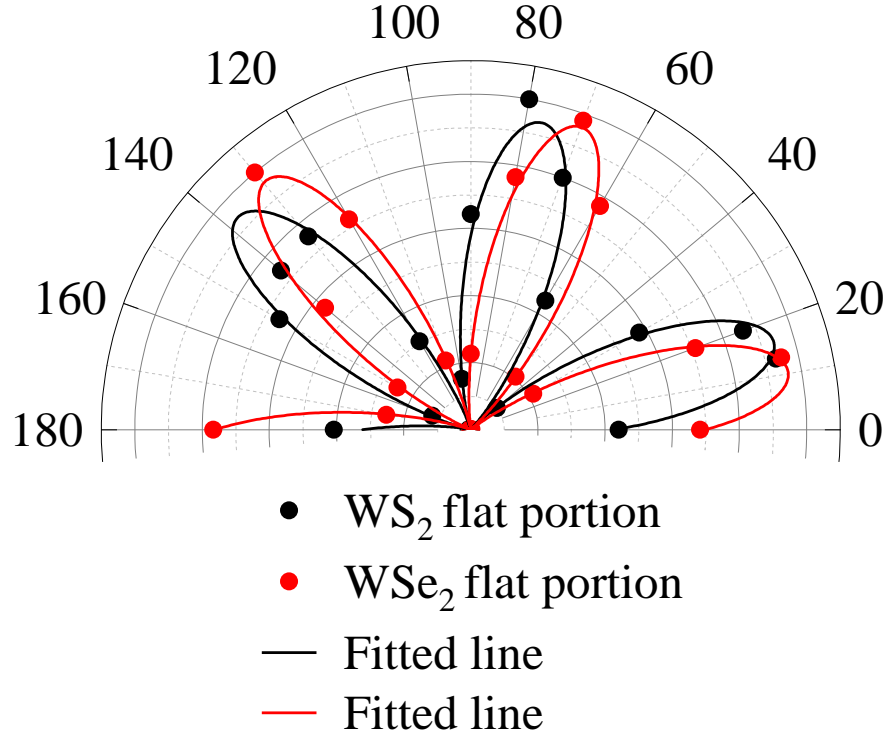
³Currently at Department of Physics, Emory University, Atlanta, USA

⁴Materials Science and Engineering, School for Engineering of Matter,
Transport and Energy, Arizona State University, Tempe, Arizona 85287, United States

^{||}These authors contributed equally

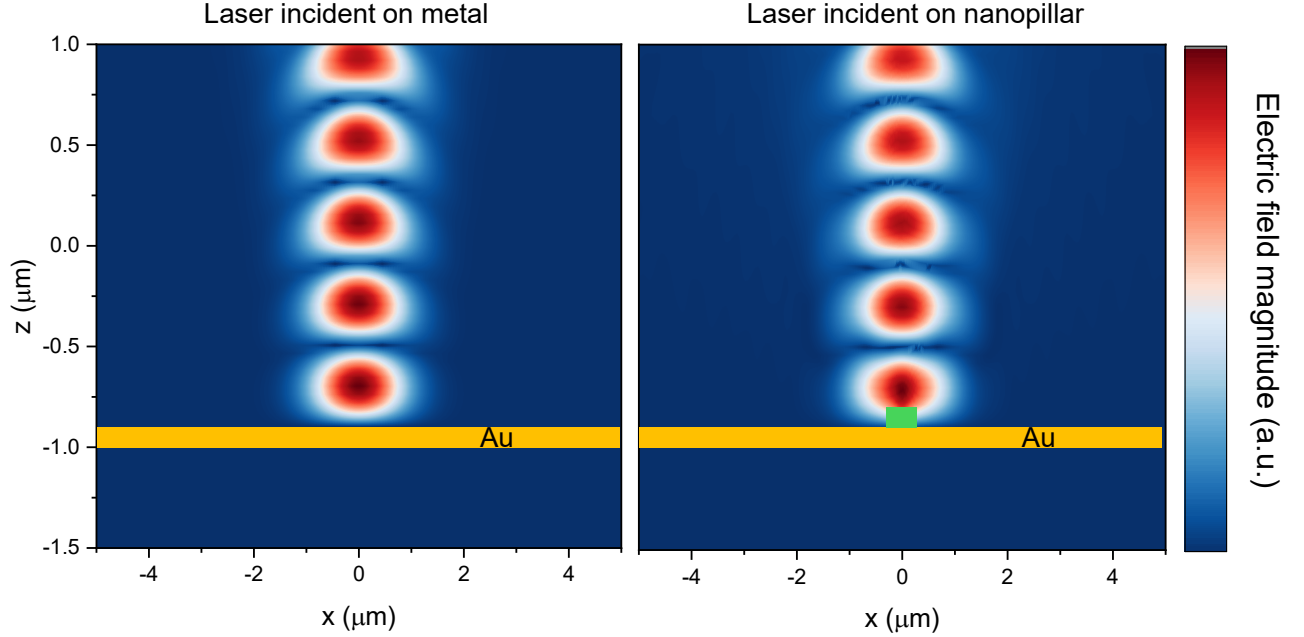
*Corresponding author, email: kausikm@iisc.ac.in

Supporting Information 1 Polarization resolved SHG measurement



Supporting Figure 1: **Polarization resolved SHG measurement:** Red circles show the SHG intensity from the WS₂ monolayer, and black squares show SHG intensity from WSe₂ monolayer. Solid traces are fit to the data. Fit gives a relative twist angle of $\sim 6^\circ$ between the two monolayers.

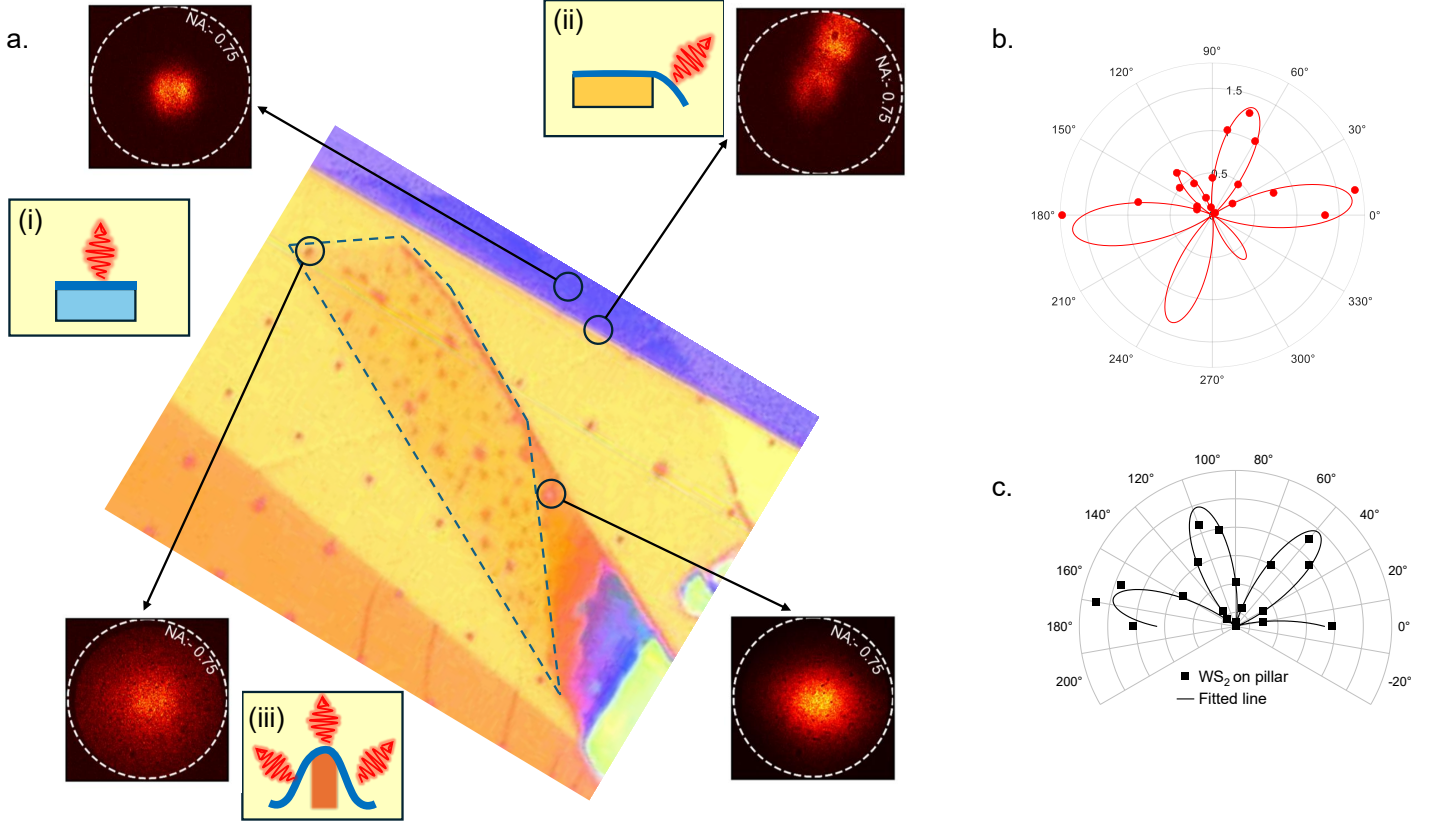
Supporting Information 2 SHG enhancement on nanopillar compared to gold substrate



Supporting Figure 2: **Gaussian laser beam incident on a gold substrate and nanopillar:** Left: Presence of a reflective coating on the substrate causes nodes and antinodes to form in the electric field strength above the surface of the gold. Right: The top of the nanopillar is near the node of the Gaussian laser beam incident on the substrate.

Enhancement of SHG intensity on the nanopillar compared to the flat portion on gold can be attributed to two mechanisms. First is the formation of an antinode of the electric field strength near the gold surface due to the reflection of the laser beam and subsequent phase flip. This is evident in the FDTD simulation shown in Supporting Figure 2 (left). This causes the electric field at the monolayer location to be of minimum intensity and thus reduces the SHG intensity. On the other hand, the node of the electric field lies closer to the top of the nanopillar, giving rise to increased SHG signal from this region [Supporting Figure 2 (right)]. Second, the presence of strain on the monolayer at the nanopillar can enhance the SHG intensity, as shown in the literature [1–3].

Supporting Information 3 Far-field SHG radiation pattern from different regions of the sample

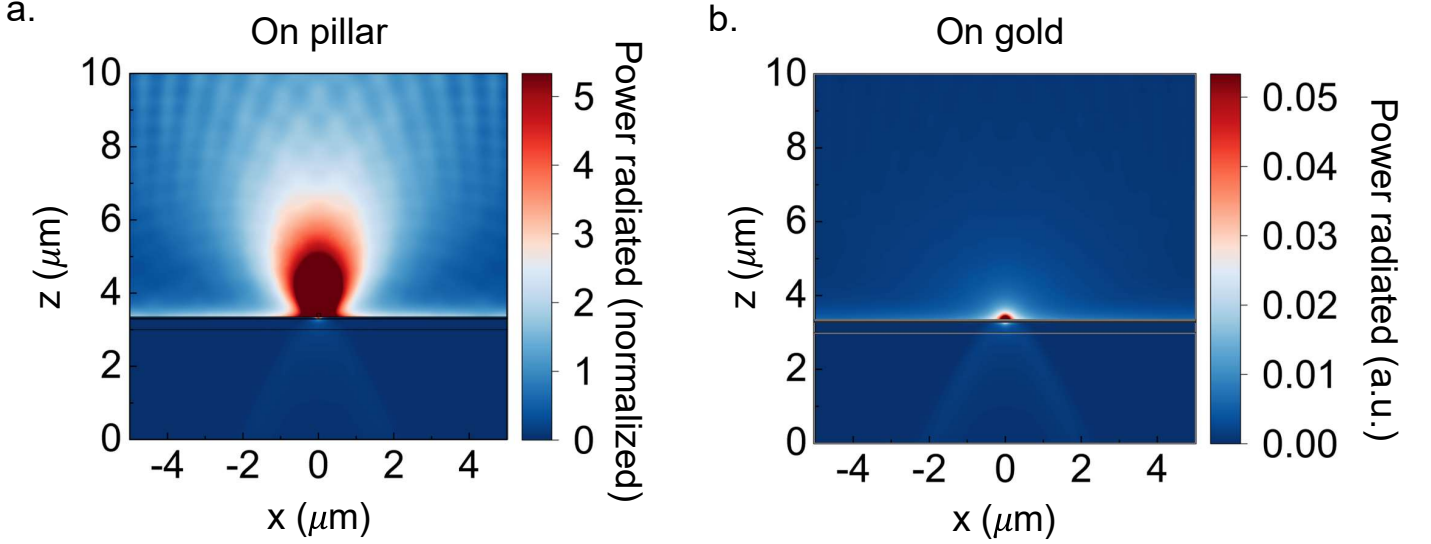


Supporting Figure 3: **Far-field SHG intensity pattern and SHG polar plot from different regions of the sample:** (a) Far-field SHG intensity pattern from monolayer on SiO₂, monolayer on the gold-strip edge, and heterobilayer on two nanopillars are shown. (b) Polarization-resolved SHG signal plot for the region where the monolayer bends over the gold line edge. (c) Polarization-resolved SHG signal plot for WS₂ on the nanopillar.

Supporting Figure 3a shows the far-field SHG signal pattern from different regions of the sample. We take the radiation pattern of the monolayer on flat SiO₂ [schematically shown in Supporting Figure 3a inset (i)] as a reference to compare with other regions. Note that for the region where the monolayer resides on the edge of the gold line, the monolayer falls over on one side of the edge, resulting in anisotropic topography. This should result in a change in the direction of radiation from the monolayer towards higher angles in one particular direction normal to the edge of the gold line [Supporting Figure 3a inset (ii)]. This is evident in the

far-field radiation pattern, which shows radiation in one direction predominantly, and matches the direction of the slant portion of the monolayer falling from the gold line edge. Compared to this, the topography of the monolayers on and around the nanopillar is expected to be isotropic in geometry. In such a case, we do not expect a preferred direction of radiation, but SHG signal over higher angles is expected isotropically [Supporting Figure 3a inset (iii)]. Accordingly, the far-field radiation pattern from the nanopillars maintains an isotropic circular shape but with increased angular size resulting from the slant portions of the monolayers around the nanopillar. We see a distortion in the polarization resolved SHG intensity polar plot from the gold line edge due to unidirectional strain (Supporting Figure 3b). In contrast to this, polarization resolved SHG plot from pillar location, as shown in Supporting Figure 3c, does not show any such distortion and is similar to the case of monolayer on flat surface (Supporting Information 1). This suggests that the monolayers on the nanopillar experience isotropic strain with no preferred direction. The maintained isotropy of both the far-field radiation pattern and the polarization resolved SHG plot confirms that the isotropic strain from the nanopillar maintains the isotropy of the sample and thus of moiré pockets on the nanopillar as well.

Supporting Information 4 FDTD simulation for excitons on pillar versus on gold substrate

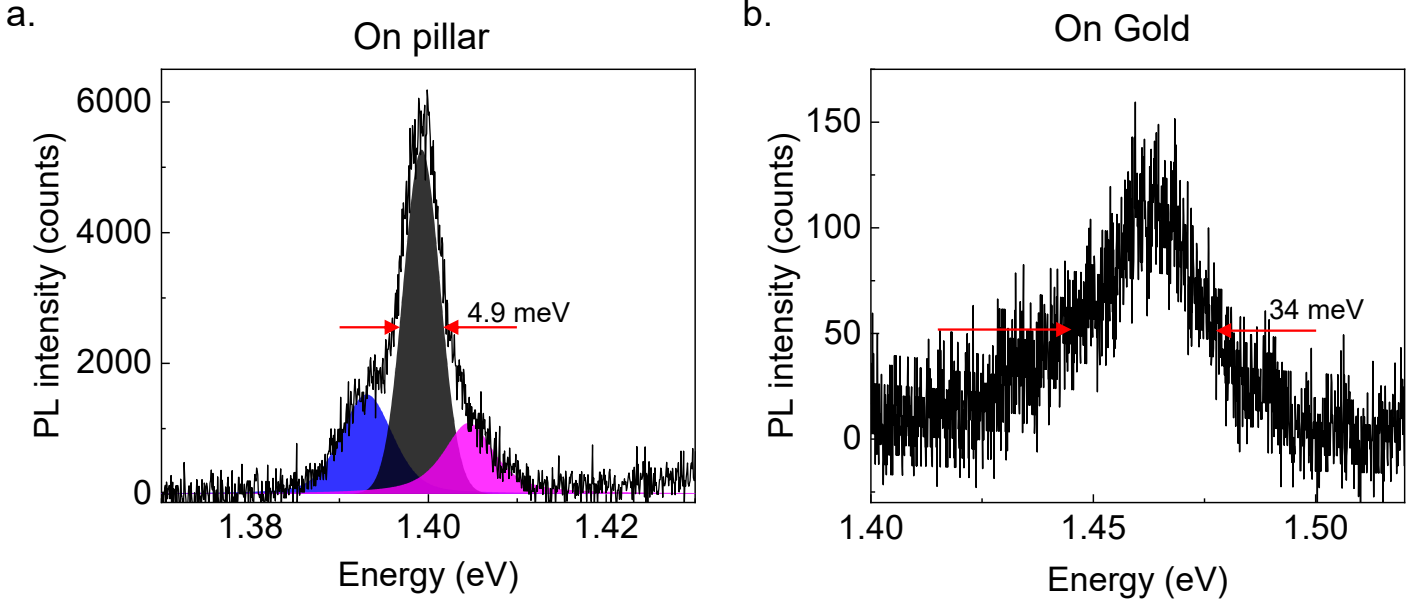


Supporting Figure 4: **FDTD simulation for excitons on pillar versus on gold substrate:** (a) Radiation pattern from excitons situated in the monolayer placed on the nanopillar. (b) Radiation pattern from excitons situated in the monolayer placed on the gold-coated substrate. Both the color plots are scaled such that they correspond to the same excitation laser power.

As discussed in Supporting Information 2, the incident laser beam on the gold surface results in an antinode near the surface. Accordingly, the excitation power seen by the monolayer and consequently its absorption is a lot less when placed directly on the gold-coated substrate compared to on top of the nanopillar. In Supporting Figure 4, results from FDTD simulation for excitons on a nanopillar versus on a gold surface are shown, under the same incident power. The effect of the lack of absorption in a monolayer directly placed on gold is already included in the results. Note that the scale bar for the plot of the exciton radiating from the gold surface is 100 times lower than the scale bar for the plot of the exciton on the nanopillar. Therefore, we conclude that the radiative emission from the monolayer touching the gold surface is quenched significantly compared to the monolayer placed on the nanopillar. Note that this result is

without considering the non-radiative exciton transfer to gold, which will make the quenching process even more prominent in the experiment.

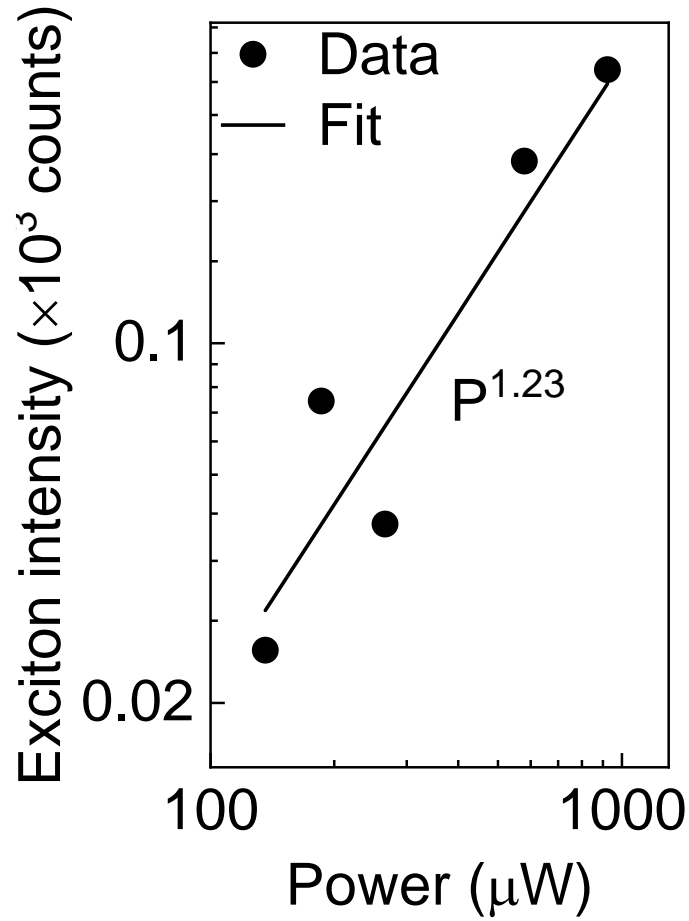
Supporting Information 5 Comparison of moiré emission from nanopillar versus from flat gold region



Supporting Figure 5: **Comparison of moiré emission from nanopillar versus from flat gold region:** (a) PL from heterobilayer on the nanopillar from another sample is shown with moiré exciton linewidth of ~ 4.9 meV. (b) PL from heterobilayer on flat gold surface from the same sample as (a).

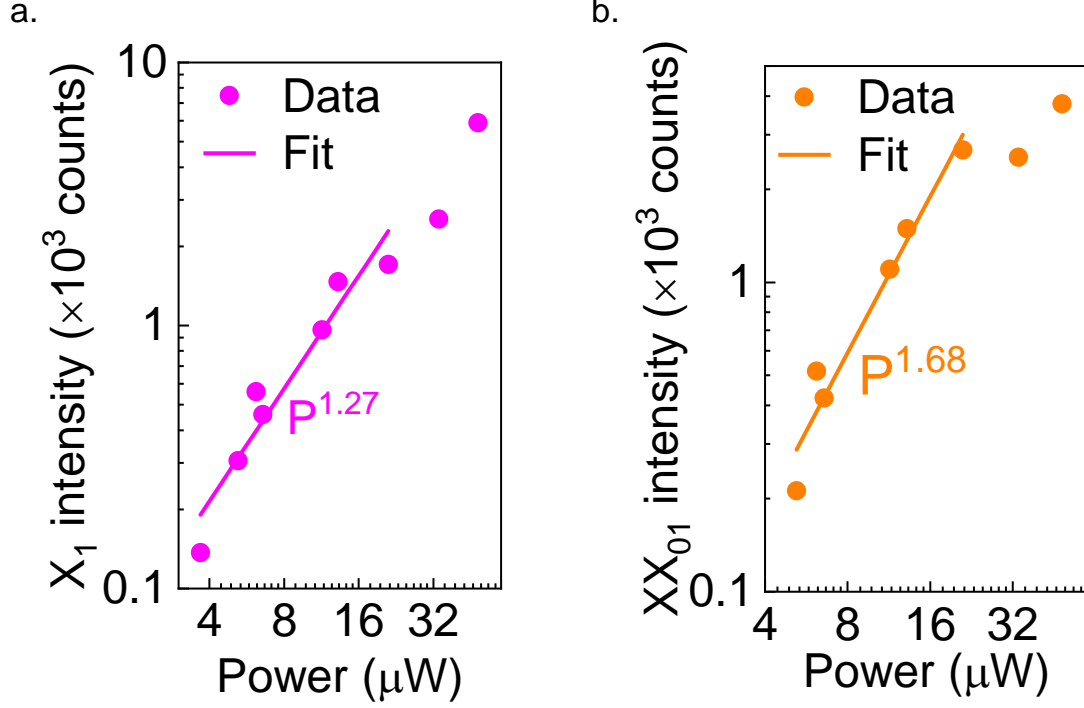
Supporting Figure 5a shows sharp emission (linewidth of 4.9 meV) from the heterobilayer on the nanopillar of another sample. We note that this is red-shifted (and significantly narrower) compared to the emission from the heterobilayer on the flat gold region of the same sample, as shown in Supporting Figure 5b. This redshift likely comes from the strain-induced band gap-lowering effect, which is also shown in intralayer excitons at room temperature in Figure 3 of the main text.

Supporting Information 6 Superlinearity of exciton from another sample



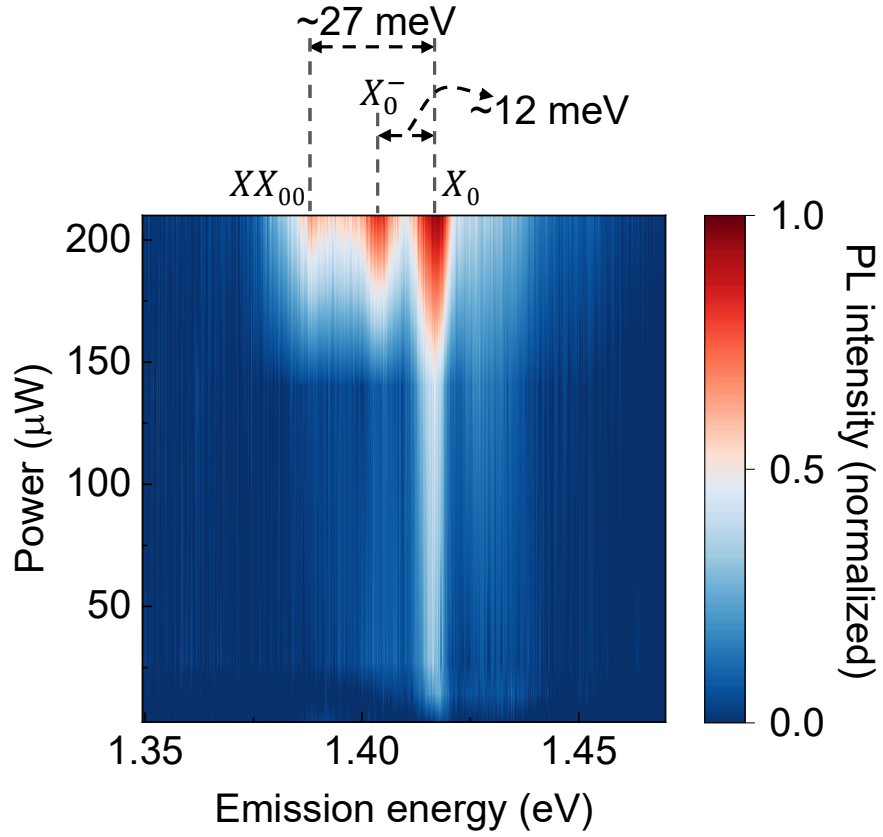
Supporting Figure 6: **Superlinearity of exciton from another sample:** Black circles show the PL intensity of the exciton peak after fitting, and the line is a power law fit to the data. Fit gives a value of $\gamma=1.23$.

Supporting Information 7 Power law coefficients of peaks X_1 and XX_{01}



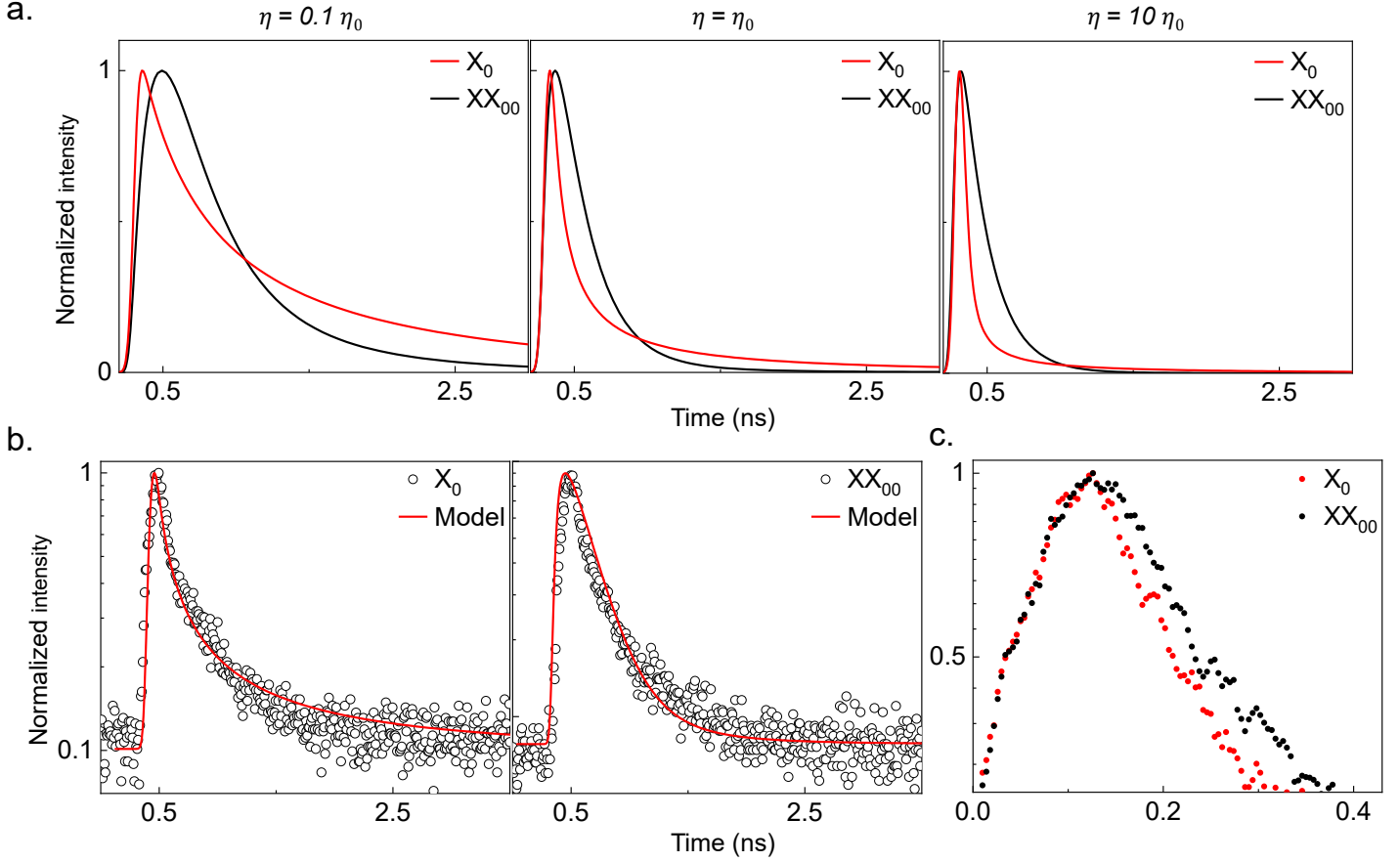
Supporting Figure 7: **Power law coefficients of peaks X_1 and XX_{01} :** (a) PL intensity versus power plot for the peak X_1 . Fit to the data gives $\gamma=1.27$. (b) PL intensity versus power plot of the peak XX_{01} . Fit to the data gives $\gamma=1.68$.

Supporting Information 8 Data from another sample showing stabilized moiré trion and biexciton



Supporting Figure 8: **Sample showing higher biexciton binding energy and lower dipolar repulsion:** Power dependent PL color plot of a sample showing biexciton (binding energy of ~ 27 meV), trion (binding energy of ~ 12 meV), and exciton.

Supporting Information 9 Rate equations and lifetime measurements of the exciton (X_0) and biexciton (XX_{00})



Supporting Figure 9: **Solutions of rate equations and lifetime measurement of the exciton (X_0) and biexciton (XX_{00}):** (a) Solutions of the rate equation for different values of exciton to biexciton conversion rates (η). (b) Measured TRPL data for the exciton and biexciton (black circles) and fitting from the rate equations (red trace). (c) Zoomed in view of the overlaid exciton and biexciton TRPL data.

We model the exciton population $[N_x(t)]$ and biexciton population $[N_{xx}(t)]$ through coupled

rate equations as follows:

$$\frac{\partial N_x(t)}{\partial t} = g(t) - \frac{N_x(t)}{\tau_x} - 2\eta N_x^2(t) + \frac{N_{xx}(t)}{\tau_{xx}^r} \quad (1)$$

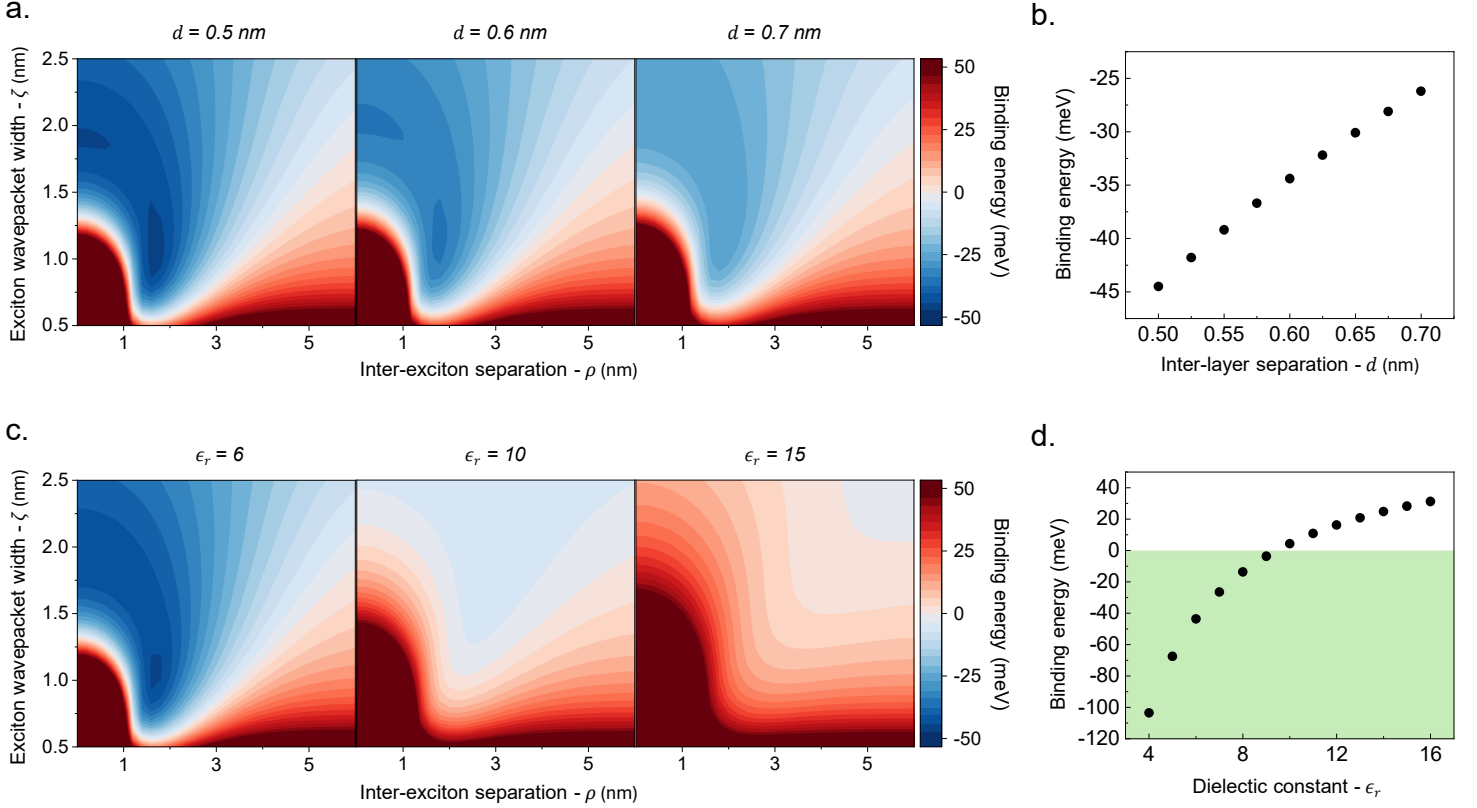
$$\frac{\partial N_{xx}(t)}{\partial t} = \eta N_x^2(t) - \frac{N_{xx}(t)}{\tau_{xx}} \quad (2)$$

where τ_x is the exciton lifetime, τ_{xx} is the biexciton lifetime with τ_{xx}^r being its radiative component, and η quantifies the rate of exciton to biexciton conversion. The rate of generation of excitons by a Gaussian laser pulse is given by $g(t) \propto e^{-\frac{1}{2}(\frac{t-\mu}{\sigma})^2}$ where σ is the width of the pulse and is related to its FWHM (59 ps) as $\text{FWHM} = 2.355\sigma$.

Supporting Figure 9a shows the solutions of these equations for different values of η with other parameters constant. We note that as the rate of exciton to biexciton conversion decreases, the decay curve of the biexciton becomes broader since the biexciton formation is delayed. Another interesting observation is the non-monexponential shape of the decay curve. Due to the presence of nonlinear terms in the coupled rate equations, we do not expect the experimental data to show a mono-exponential decay.

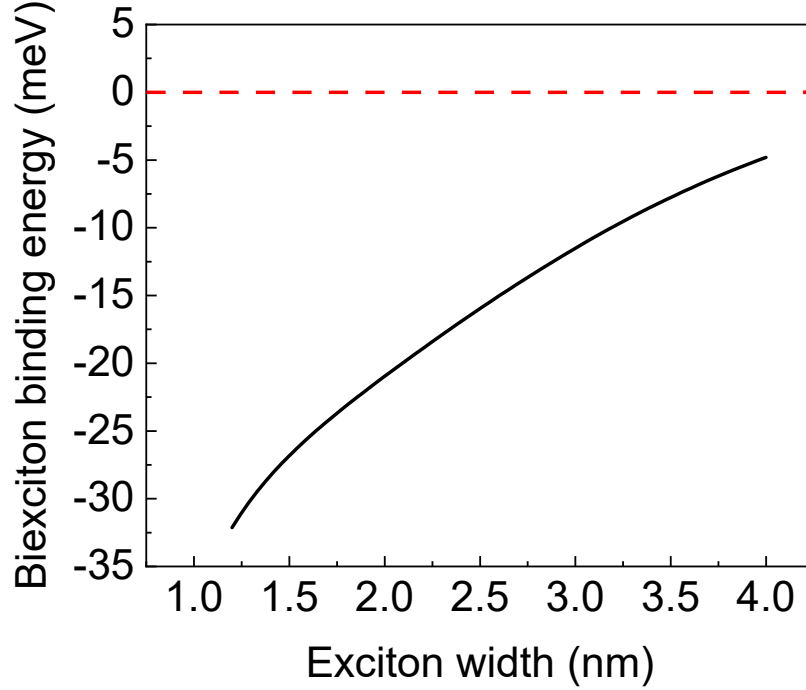
This is confirmed by the experimental data for exciton and biexciton TRPL data in Supporting Figure 9b. Both the exciton and the biexciton show a non-monexponential decay rate, which supports the coupling of their rate equations through nonlinear terms. At steady state ($\frac{\partial N_{xx}(t)}{\partial t} = 0$), $N_{xx} = \eta\tau_{xx}N_x^2$. Therefore, the value of $\eta\tau_{xx}$ can be estimated from PL measurements performed with a CW laser as $\eta\tau_{xx} \sim 10^{-3}$. Taking this as a starting point, we were able to simultaneously fit both the exciton and biexciton to the experimental data with the solutions of the rate equations with the fitting constants $\tau_x = 4$ ns, $\tau_{xx} = 0.34$ ns (with radiative part $\tau_{xx}^r = 10$ ns), and $\eta = 5.71 \times 10^6$ s⁻¹. This shows that due to the nonlinear nature of the coupled differential equations, the decay rates measured in the TRPL experiment (~ 50 -100 ps here) can be much faster than the radiative lifetimes of the exciton and the biexciton. From the values of fitting parameters, $\tau_{xx} < \tau_x$, but both the experimental data and solutions to the rate equations show that the actual decay for the excitons is faster because of their conversion to biexcitons. Supporting Figure 9c shows a zoomed-in view of the exciton and biexciton TRPL data depicting the delayed biexciton emission, confirming that the exciton population is being converted to the biexciton population.

Supporting Information 10 Biexciton stabilization with varying parameters



Supporting Figure 10: **Biexciton binding energy calculation with varying constants:** (a) Biexciton binding energy as a function of exciton wavepacket width (ζ) and inter-exciton separation (ρ) with different values of interlayer separation (d) for a given effective dielectric constant ($\epsilon_r = 6.5$). (b) Variation of binding energy with interlayer separation for $\zeta = 1.11$ nm and $\rho = 1.8$ nm. (c) Biexciton binding energy as a function of exciton wavepacket width (ζ) and inter-exciton separation (ρ) with different values of dielectric constant (ϵ_r) keeping a fixed inter-layer separation ($d = 0.6$ nm). (d) Variation of binding energy with dielectric constant for $\zeta = 1.11$ nm and $\rho = 1.8$ nm. The green shaded portion shows the region of stability of the biexciton.

Supporting Information 11 Biexciton binding energy as a function of exciton width in a moiré well



Supporting Figure 11: **Biexciton binding energy as a function of exciton width in a moiré well:** Binding energy of the biexciton is shown with varying exciton wavepacket width (and thus moiré well size or the twist angle.) The red dashed line denotes the limit after which the biexciton becomes unstable. A relatively smaller well size (and hence, a relatively larger twist angle) stabilizes the biexciton in a more efficient way.

For a given set of materials (such as WS_2 and WSe_2 here), the moiré twist angle determines the moiré well size, potential depth, and the moiré period. A wider moiré pocket would mean a wider center of mass wavefunction of the single exciton in the pocket, which would lead to a lower energy of the exciton. Since binding energy is the difference between the energy of the biexciton and the energy of two non-interacting excitons, the magnitude of the binding energy decreases when the individual exciton energy decreases. Thus, a wider moiré pocket leads to

biexcitons with lower binding energy. The same is confirmed by varying the individual size of the exciton wavepacket in our model, as shown in Supporting Figure 11. Therefore, a relatively smaller well size (and hence, a relatively larger twist angle) stabilizes the biexciton in a more efficient way.

References

- [1] Zhizi Guan et al. “Strain-Induced Giant Second-Order Susceptibility in Monolayer WSe₂”. *Physical Review B* 111.24 (2025), p. 245423.
- [2] Sudeep Puri et al. “Substrate Interference and Strain in the Second-Harmonic Generation from MoSe₂ Monolayers”. *Nano Letters* 24.41 (2024), p. 13061.
- [3] Sehwan Chang et al. “Enhancement of Second-Harmonic Generation in a 64° Stacked WSe₂/WS₂ Heterobilayer with Local Strain”. *Nanotechnology* 35.14 (2024), p. 145201.